Precursors_cci+
ESA Climate Change Initiative (CCI)





Product Validation and Algorithm Selection Report (PVASR)

Version 2.0

Title	Product Validation and Algorithm Selection Report (PVASR)
Reference	Precursors_cci+_D2.3_PVASR_02_00
Issue	02
Revision	00
Status	Draft
Date of issue	31/07/2026
Document type	Deliverable

This work has received funding from the European Space Agency under Contract No 4000138243 and is the result of the cooperation between the partners of the Precursors_cci+ consortium.

















	FUNCTION	NAME	DATE
LEAD AUTHOR(S)	Authors	Andreas Richter Isidora Anglou Steffen Beirle Folkert Boersma Steven Compernolle Isabelle De Smedt Arka Mitra Sora Seo Tijl Verhoelst Thomas Wagner	31/07/2026
REVIEWED BY	Science Leaders	M. Van Roozendael Folkert Boersma	31/07/2026
	ESA Project Officer	Simon Pinnock	../../....
DISTRIBUTED TO	ESA Precursors_cci+ Consortium		

Table of Contents

1 Executive summary 8
2 Purpose of document 8
3 BRDF effects on LEO data 9
3.1.1 DLER climatology 9
3.1.2 GE_LER database 9
3.1.3 Comparison of DLER and GE_LER surface albedo values 11
3.1.4 Spatial resolution 16
3.1.5 Temporal representativeness 17
3.1.6 Directionality 18
3.2 Impact of directional reflectance on cloud parameters 21
3.3 Impact of directional reflectance on NO_2 retrievals 22
3.4 Impact of directional reflectance on HCHO retrievals 24
3.5 Validation 25
3.5.1 Clouds 25
3.5.2 NO_2 28
3.6 Algorithm selection 32
4 Separation of stratosphere and troposphere for NO_2 32
4.1 Data and algorithms used 32
4.1.1 Data 32
4.1.2 Algorithms 32
4.2 Comparison 35
4.2.1 Spatial patterns 35
4.2.2 Dependency on latitude 37
4.2.3 Dependency on time of day 37
4.2.4 Distribution of tropospheric residuals over clean regions 38
4.3 Algorithm selection 39
5 GEMS NO_2 40
5.1 Data and algorithms used 40
5.2 Surface reflectance 40
5.3 Clouds 44
5.4 Separation of stratosphere and troposphere 48
5.5 Validation 49

5.6 Algorithm selection 51
6 Summary and Conclusions 51
7 References 52

List of Figures

Figure 3-1: Surface reflectivity on 16 December 2020 for TROPOMI (orbit 16459, upper panels) and for 16 July 2021 (orbit 19466, lower panels), as predicted by the GE_LER product (445 nm) and DLER product (440 nm), and their differences (GE_LER-DLER) 12

Figure 3-2: Normalised histograms of surface albedo from TROPOMI observations on 16 December 2020 (top) and 16 July 2021 (bottom), as provided by the GE_LER and DLER products at 440 nm. The histograms are normalised such that the total area under each histogram equals one. 13

Figure 3-3: Lambertian-equivalent reflectance on 16 December 2020 for TROPOMI orbit 16459 (upper panels) and for 16 July 2021 (orbit 19466, lower panels), as predicted by the DLER product (340 nm) and GE_LER product (344 nm), and their differences. 14

Figure 3-4: Probability density histograms of surface albedo from TROPOMI observations on 16 December 2020 (top) and 16 July 2021 (bottom), as provided by the GE_LER and DLER products at 340 nm. 15

Figure 3-5: Zoomed-in maps of surface reflectance over the Amazon Basin for TROPOMI orbit 16462 on 16 December 2020, derived from the DLER product (440 nm) and the GE_LER product (445 nm), and the corresponding differences between the two datasets. 16

Figure 3-6: (a) Minimum LER from the GE_LER database, (b) minimum LER from the DLER database, (c) difference between GE_LER and DLER. Both minimum LERs are selected for the month of November at 440 nm (DLER) and at 435-355 nm (GE_LER) for the strait of Gibraltar, parts of Spain, Morocco, and the western Mediterranean. 16

Figure 3-7: Temporal variability in surface albedo derived on orbit basis from the S5P DLER and the OMI LER, spatially averaged at 0.2° resolution, and the monthly S5P minLER of the DLER database (v2.2 at 440 nm), and from the GE_LER database for H2O (v3.3.1, 435-455 nm) , for an agricultural area in the Po Valley (45.3°N, 9.7°E). The spatial resolution of the S5P DLER and minLER climatologies are 0.125°x0.125° and the resolution of the OMI climatology is 0.5°x0.5°. The DLER shown in the figure is consistent with TROPOMI NO2 v2.4 retrieval, which is based on the S5P minLER v1.0 climatology (from the DLER database, 3 years of TROPOMI data), while the figure shows the DLER minLER v2.2 (7 years of TROPOMI data), but we do not expect significant variation between the two versions. 17

Figure 3-8: Surface reflectivity values at 440 nm as a function of TROPOMI viewing zenith angle over the Amazon (0°-10°S, 55°E – 65°E) and Europe (4°E- 17°E, 47°N-55°N, excluding water pixels) from the DLER (blue) and GE_LER (orange) databases for December 2020 and July 2021. For comparison, the MINLER values of each database are also shown (in lighter blue and orange). 18

Figure 3-9: Probability density function of DLER and GE_LER differences for December 2020 and July 2021 over the Amazon (0°-10°S, 55°E – 65°E) and Europe (4°E- 17°E, 47°N-55°N, excluding water pixels) for 440 nm.....19

Figure 3-10: Surface reflectivity values at 340 nm as a function of TROPOMI viewing zenith angle over the Amazon (0-10°S, 55°E – 65°E) and Europe (4°E- 17°E, 47°N-55°N, excluding water pixels) from the DLER (blue) and GE_LER (orange) databases for December 2020 and July 2021. For comparison, the minLER values of each database are also shown (in lighter blue and orange). 20

Figure 3-11: Probability density function of DLER and GE_LER differences for December 2020 and July 2021 over the Amazon (0°-10°S, 55°E – 65°E) and Europe (4°E- 17°E, 47°N-55°N, excluding water pixels) for 340 nm.....21

Figure 3-12: Surface albedo, cloud fraction and cloud pressure at 758 nm, and surface albedo and cloud fraction at 440 nm comparison between TROPOMI NO_2 product v2.4 and v2.3.1 over South America on 16 December 2020 (Orbit 16462).....22

Figure 3-13: NO_2 AMF and tropospheric column differences between TROPOMI NO_2 product v2.4 and v2.3.1 over South America on 16 December 2020 (Orbit 16462).....23

Figure 3-14: Surface albedo (340nm), HCHO AMF and tropospheric column comparison between test daily HCHO columns using DLER and minLER for the retrieval over South America on 15 January 2020.....24

Figure 3-15. Top. Left. Monthly dispersion (1/2 IP68) of CLOUD ROCINN_CAL CTH minus FRESCO CH, per station. The version upgrade from UPAS v1 to UPAS v2 on 2020/07/13 is indicated by a black dashed line. Right. Dispersion over the full time range. Figure taken from ROCVR#17 (Lambert et al., 2022). Bottom: same but for CLOUD ROCINN_CRB CH minus FRESCO CH. 26

Figure 3-16 Comparison of S5P FRESCO-S cloud height with ACTRIS Cloudnet Cloud mean height. Left: FRESCO OFFL v2.2-2.3. Right: FRESCO RPRO v2.4. The temporal range is 2021-07-01 to 2022-07-17, when OFFL v2.2-2.3 was active. Selected sites are Hyytiala, Norunda, Lindenberg, Chilbolton, Juelich, Palaiseau, Munich, Bucharest, Granada.....28

Figure 3-17: Data density (as grey scale) of the differences between S5P and PGN total NO_2 as a function of PGN total NO_2 (on the vertical axis) for the PAL v2.3.1 data (left-hand panel) and the v2.4 data (right-hand panel). Estimated bias (mean difference) and dispersion (standard deviation) per VCD bin are indicated in red and magenta, respectively. Results are roughly identical up to ~13 Pmolec/cm^2, above which v2.4 demonstrates a slightly more negative bias, albeit with a clearly reduced dispersion. 29

Figure 3-18: Temporal subset of the S5P vs. PGN comparisons at City College, New York, for the PAL v2.3.1 data in the top panel and for the v2.4 data in the bottom panel. 30

Figure 3-19: Scatter plots and histograms corresponding to the analysis at City College, New York, for PAL v2.3.1 on the left-hand side and v2.4 on the right-hand side. Most notable are the reduced dispersion but increased multiplicative underestimation in v2.4. 31

Figure 4-1: Slope of the linear increase of stratospheric NO2 for different months as a function of latitude, derived from a linear fit to EMAC data. Literature values are added as crosses. The dashed line displays the parameterization of Eq. 1. 34

Figure 4-2: Monthly mean V_{strat} (top) and TR (bottom) for the GEMS v3 operational product. 35

Figure 4-3: Monthly mean V_{strat} for the investigated algorithms applied on GEMS data, and the TROPOMI operational product. Colorbar as in Fig. 4.1.....36

Figure 4-4: Monthly mean TR for the investigated algorithms applied on GEMS data, and the TROPOMI operational product. Colorbar as in Fig. 4.1.....36

Figure 4-5: Monthly mean stratospheric VCD as a function of latitude. 37

Figure 4-6: Monthly mean stratospheric VCD at 34.5° N, 126.5° E as a function of time of day. Colors as in Fig. 4.5. 37

Figure 4-7; Temporal mean tropospheric VCD (May 2018-November 2021) from the TROPOMI PAL product. Black rectangles indicate the "clean" regions (Table 4.1). 38

Figure 4-8: Frequency distribution of TRs for the investigated reference regions. Colors as in Fig. 4.5. 39

Figure 5-1: Scatterplots of satellite vs. co-located ground-based NO_2 tropospheric VCDs for (a) the GEMS L2 v3.0 product using the GEMS L2 surface reflectance observations, (b) the original GEMS IUP-UB product using the TROPOMI LER v1, and (c) the GEMS IUP-UB product using the GEMS L2 v3.0 reflectance data. 41

Figure 5-2: Monthly average of the surface reflectance products for October 2022 at 00:45 UTC, 03:45 UTC, and 06:45 UTC for GEMS L2 v3.0 (top row, GEMS L2 BSR), GEMS IUP-UB (middle row, TROPOMI LER), and the difference of the GEMS v3.0 – GEMS IUP-UB surface reflectance products (bottom row). 42

Figure 5-3: Surface reflectance maps of the TROPOMI LER v2-2 (top row), the MODIS BRDF-based LER (middle row), and their difference (bottom row) for 15 January 2023 for the 01:45, 03:45, and 05:45 UTC GEMS observation time.....43

Figure 5-4: Time series of the surface reflectance of the TROPOMI LER v2-2 (blue) and the MODIS BRDF-based LER (orange) for a selected pixel in Seoul (left), Singapore (middle), and central India (right) for one individual day in each season (15 January, 15 April, 15 July, and 15 October 2023). 44

Figure 5-5: (left) Cloud fraction maps on 15 April 2021 for the GEMS L2 v3.0 for the 03:45 UTC observation and the TROPOMI v2.4 product and their differences. (right) Corresponding distribution histograms of the cloud fractions.....45

Figure 5-6: Cloud pressure maps on 15 July 2024 of the GEMS L2 v3.0 for the 03:45 UTC observation and the TROPOMI v2.6 FRESCO product (left) and the O_2-O_2 product (right) and their differences.....46

Figure 5-7: Cloud fraction distributions for 15 April 2024 for the 3:45 UTC scan for the operational GEMS L2 v3.0 O_2-O_2 cloud fraction (green), the GEMS IUP-UB cloud radiance fraction in the NO_2 window (blue), and the collocated TROPOMI cloud radiance fraction in the NO_2 window for that day (yellow).....47

Figure 5-8: Cloud fraction for 15 April 2023 of the scans 00:45 UTC (left column), 03:45 UTC (middle), and 06:45 UTC (right) for the GEMS IUP-UB cloud algorithm based on the TROPOMI LER v2-2 (top row) and the MODIS BRDF-based LER (middle row), and their differences (bottom row). 48

Figure 5-9: Diurnal variation in median stratospheric NO_2 VCDs at the Pandora Seoul site for the TROPOMI product, shown as the black dot, the TM5 model stratospheric VCDs in green, used for

the TROPOMI product, the GEMS IUP-UB STREAM-based product in light blue, and the GEMS L2 v2.0 (left plot) and v3.0 (right plot) product based on the method from Bucsela et al. (2013) in dark blue. 48

Figure 5-10: Map of Pandora and MAX-DOAS instruments in the GEMS observation domain used for analysis. 49

Figure 5-11: Diurnal variation in the median relative differences of the GEMS IUP-UB NO_2 product using the GEMS BSR v3.0 (top left), the TROPOMI LER v1-1 (top right), the TROPOMI LER v2-2 (bottom left), respectively the MODIS BRDF-based LER (bottom right), and the ground-based stations for the different seasons. The overall median for each time bin, including the individual differences of all sites, is shown in green, red, pink, and blue. The individual station median in the time bin is color-coded. Box bounds mark the 25% and 75% quantiles. Whiskers represent the 5% and 95% quantiles. 50

List of Tables

Table 3-1: DLER and GE_LER specifications 11

Table 3-2. Validation statistics of S5P CLOUD OCRA/ROCINN_CAL cloud top height (CTH) versus ACTRIS Cloudnet CTH. To obtain the overall bias and dispersion, first the QI is calculated per station (median difference, median relative difference and ½ of the central 68-interpercentile of the difference), then the median over all stations is taken. Table adapted from [ROCVR#17], Table 19. The distinction between low and high clouds is taken at Cloudnet CTH=4 km. 26

Table 3-3. Validation statistics of S5P CLOUD OCRA/ROCINN_CRB cloud height (CH) versus ACTRIS Cloudnet cloud mean height (CMH). To obtain the overall bias and dispersion, first the QI is calculated per station (median difference, median relative difference and ½ of the central 68-interpercentile of the difference), then the median over all stations is taken. Table adapted from [ROCVR#17], Table 19. The distinction between low and high clouds is taken at Cloudnet CTH=4 km. 27

Table 4-1: “Clean” reference regions. 38

Table 5-1: Algorithm choices for the Precursors GEMS NO_2 product. The comment column gives the reason for the choice 51

1 Executive summary

The product Validation and Algorithm Selection Report (PVASR) provides a complete report of the results of the algorithm Round Robin intercomparison as the basis for further algorithm development during the Precursors CCI+ project. In this second issue, additional topics not covered in the first issue, but addressed in the second phase of the project, are discussed. This includes

1. A critical evaluation of directional effects of the surface reflectivity and its representation in available databases.
2. An assessment of different approaches to the separation of stratospheric and tropospheric signals in GEMS NO_2 retrievals.
3. A systematic analysis and comparison of retrieval settings for the GEMS NO_2 Precursor product.

The main findings of the Round Robin are that the two databases currently used in satellite retrievals to account for the directionality of the surface reflectance, GE_LER and DLER, agree qualitatively but not quantitatively. Using directionally dependent surface reflectances has a moderate impact on tropospheric NO_2 columns and a small effect on HCHO columns. Part of the effect is from direct clear-sky AMF changes, another part from indirect effects of changes in the cloud parameters. The switch to directionally dependent surface reflectances in the TROPOMI processor improved validation results for cloud top heights, but other changes were introduced at the same time, making firm conclusions difficult.

For the stratospheric NO_2 algorithms, both model-based and data-driven methods perform well in principle. The best option appears to be a model-based approach with empirical correction to account for model deficiencies.

For the GEMS NO_2 product, problems with the operational cloud product have been identified that can, at least in part, be corrected by replacing the cloud fraction algorithm with an alternative implementation. The operational surface reflectance product should not yet be used as its application deteriorates validation results. Applying the TROPOMI minLER climatology yields good validation results, which can be further improved by introducing MODIS BRDF-based DLER values.

Based on the Round Robin results, choices have been made and documented for the GEMS NO_2 product. The implementation details are described in the respective ATBDs.

2 Purpose of document

This document reports on the results of the Round Robin exercise for the NO_2 and HCHO products performed in the second phase of the Precursors CCI+ project. The aim of the Round Robin was to study the sensitivity to specific choices made for the algorithms and input data not investigated in the first phase and to make a decision on which options to choose for the climate data records produced in the project. While some limited validation with independent measurements was performed as part of the Round Robin, the main part of the validation will be done on the CDR products and will be reported in the Product Validation and Intercomparison Report (PVIR).

The document has three main parts: A detailed investigation of BRDF effects in section 3, a comparison of different stratospheric correction algorithms in section 4, and an evaluation of different retrieval settings for the GEMS NO_2 data set. The details on the consolidated algorithms can be found in the ATBDs for the respective products.

3 BRDF effects on LEO data

We compare here two state-of-the-art databases that describe surface reflectivity as a function of viewing geometry for the TROPOMI sensor: the directionally-dependent Lambertian Equivalent Reflectivity (DLER) climatology, and the geometry-dependent Lambertian-equivalent reflectivity database (GE_LER). The databases have been developed independently at KNMI and DLR from the same TROPOMI reflectance measurements.

3.1.1 DLER climatology

A climatological directionally-dependent Lambertian-equivalent reflectivity (DLER) climatology has been developed by KNMI for each calendar month for 21 specific wavelengths at a resolution of 0.125° x 0.125° (Tilstra et al., 2024). The climatology is based on TROPOMI level-1 reflectance measurements (v2.1) from 2018 until 2023 (5 years worth of data). The effective LER is determined by minimizing the differences between observed reflectances and simulated reflectances that depend on scene albedo, while accounting for reduced atmospheric transmission due to scattering and absorption (by O_3, NO_2, and O_2-O_2 at 440 nm). Over land, the DLER climatology contains values of the minimum LER (A_{LER}), and 4 coefficients for each cell that, together with the viewing angle (θ_v) provide the directional LER. Over sea, the climatology only provides the minimum LER. For areas that are potentially covered by snow or ice, the climatology provides two sets of values: one climatology for snow/ice free scenes, and one for scenes when they are covered by snow or ice. When looking-up the climatological value for a particular day, the user can select either set of values depending on whether ancillary data indicates that a scene is covered by snow or ice or not.

3.1.2 GE_LER database

DLR developed a directionally-dependent Lambertian-equivalent reflectivity database, referred to as GE_LER (Geometry-dependent Effective Lambertian Equivalent Reflectivity), building on TROPOMI level-1 reflectance measurements (v2.1). The GE_LER product is retrieved using a machine-learning framework, the FP_ILM (Full Physics Inverse Learning Machine), applied over the same wavelength fitting windows as those used in operational trace gas and cloud property retrievals.

The effective surface albedo retrieval relies on the FP_ILM algorithm, a neural network–based approach that combines smart sampling strategies with dimensionality reduction techniques. This methodology is already implemented in the operational TROPOMI O_3 vertical column density and cloud retrieval algorithms (Loyola et al., 2020). The FP_ILM framework consists of two main components: (i) offline neural network training and (ii) online application to measured data. Once trained, the neural network operator can be applied to observations with very high computational efficiency, as the retrieval reduces to a series of matrix multiplications. During the offline training phase, simulated reflectance spectra are generated using the VLIDORT model (Spurr et al., 2008)

for each trace gas and cloud retrieval window, based on a smartly sampled state space (Loyola et al., 2016). Dimensionality reduction is subsequently applied, either through principal component analysis (PCA) or via DOAS polynomial coefficients, to efficiently represent the spectral information. The trained neural network is then used to retrieve GE_LER albedo from measured TROPOMI reflectance spectra.

The GE_LER climatology is constructed by filtering out scenes affected by clouds and aerosols, using thresholds of cloud fraction < 0.01 and aerosol index < 1, and by excluding pixels contaminated by sun-glint or strong aerosol signals. Monthly GE_LER fields are generated on a regular latitude–longitude grid with a spatial resolution of 0.125° × 0.125°. For land and water surfaces, the monthly values are derived as the mean of the lowest 10% of LER values, while for snow and ice surfaces, the lowest 10% of LER values are excluded and the mode of the remaining distribution is used. To ensure spatial and temporal completeness, remaining gaps are filled in a post-processing step using valid observations from other months.

Given the close spectral range of the NO_2 and H_2O (with effective central wavelengths of 440 nm for NO_2 and 445 nm for H_2O), the GE_LER climatology derived from the S5P PAL H_2O product (Chan et al., 2022) was compared with the DLER climatology at 440 nm in this study.

Table 3-1: DLER and GE_LER specifications

	GE_LER	DLER
Level-1 input	v2.1.0	v2.1.0
Temporal representativity	Climatology based on daily estimates	Monthly climatology
Spatial resolutions	0.125° × 0.125°	0.125° × 0.125°
Relevant wavelength	445 nm (midpoint of 435-455 nm), 344 nm (mid-point of 328-359nm)	440 nm, 340 nm
Scenes rejected	Clouds, aerosols, sun-glint and solar eclipse scenes filtered out.	Clouds, aerosols, sun-glint and shadow scenes filtered out
Radiative transfer model	VLIDORT	DAK (Stammes et al., 2001)
Land	6th degree polynomial (Eq. (2)) HCHO: 7th degree polynomial	3rd degree polynomial (Eq. (1))
Water	6th degree polynomial (Eq. (2)) HCHO: 7th degree polynomial	$= A_{LER}$
Snow/ice	6th degree polynomial (Eq. (1)) HCHO: 7th degree polynomial	User selects snow/ice-free or snow/ice-climatology based on actual situation

The exact equations to derive the local DLER and GE_LER albedo values are specified with equations (1) and (2) below:

$$A_{DLER} = A_{LER} + c_0 + c_1\theta_v + c_2\theta_v^2 + c_3\theta_v^3 \quad (1)$$

$$A_{GE_LER} = A_{LER} \times (c_0 + c_1\theta_v + c_2\theta_v^2 + c_3\theta_v^3 + c_4\theta_v^4 + c_5\theta_v^5 + c_6\theta_v^6) \quad (2)$$

3.1.3 Comparison of DLER and GE_LER surface albedo values

Surface albedos derived from GE_LER and DLER were compared for selected TROPOMI orbits acquired on 16 December 2020 and 16 July 2021. Figure 3-1 presents maps of the surface albedo retrieved from both datasets together with the corresponding difference maps for representative orbits over Europe and Africa.

In general, GE_LER and DLER show similar consistent spatial patterns and comparable surface albedo ranges. Nevertheless, notable differences are evident over the polar regions, the Sahara Desert, and the open oceans. The largest discrepancies occur over highly reflective surfaces, particularly Antarctic sea ice. In this region, DLER produces a narrow range of albedo values, with

most pixels clustered between 0.95 and 1.0, whereas GE_LER exhibits a considerably broader range spanning approximately 0.7–1.0. In comparison, differences between the two datasets are relatively smaller over the Arctic, including Greenland, despite the presence of similar snow and ice-covered surfaces. Over dark surfaces, primarily the open ocean, GE_LER generally retrieves lower surface albedo values than DLER. In contrast, over the Sahara Desert, GE_LER systematically produces higher albedo values. As a result, GE_LER provides a more pronounced land–ocean reflectance contrast, which is particularly evident along coastlines such as the Mediterranean Sea and the Saharan Desert coast.

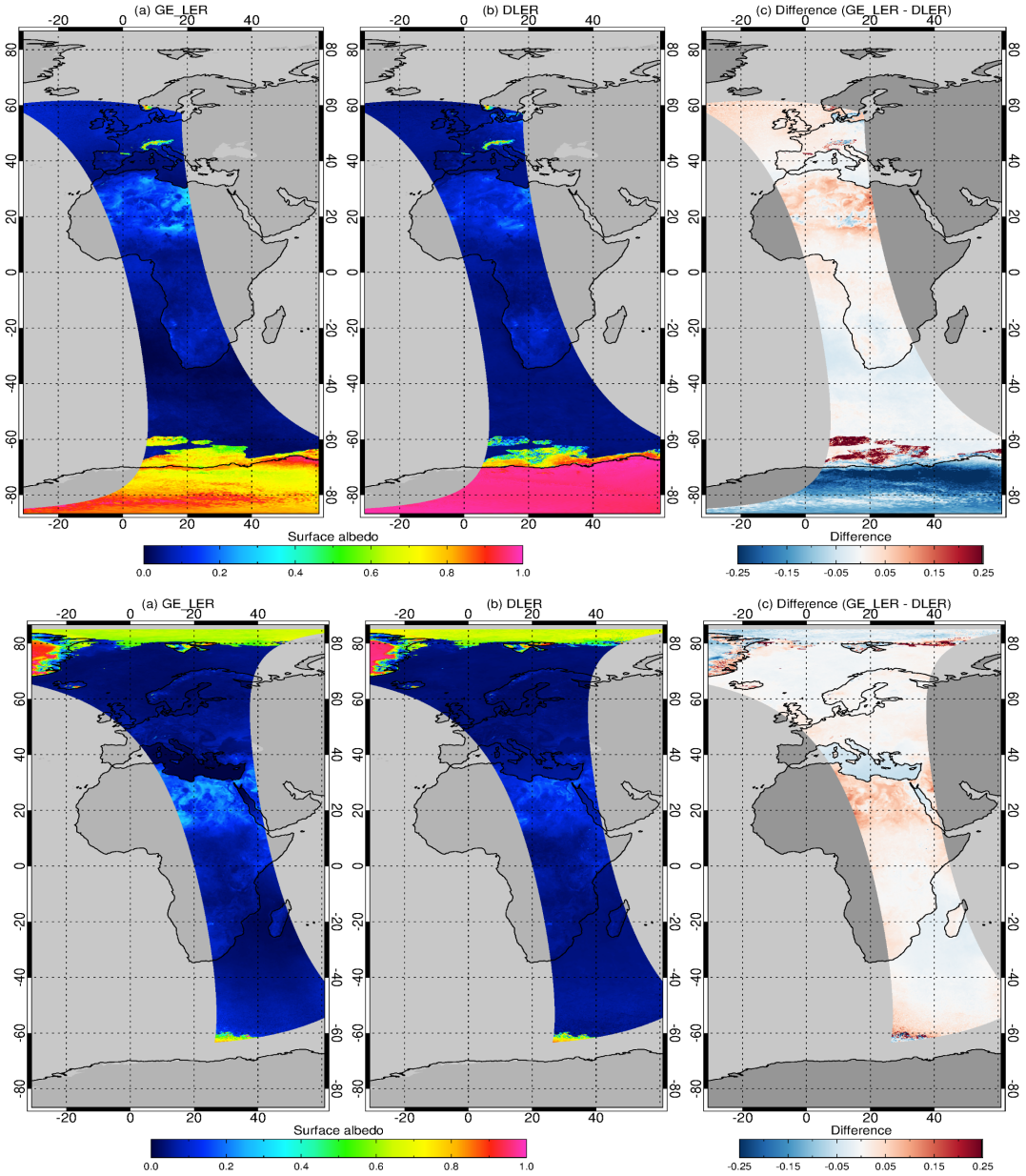


Figure 3-1: Surface reflectivity on 16 December 2020 for TROPOMI (orbit 16459, upper panels) and for 16 July 2021 (orbit 19466, lower panels), as predicted by the GE_LER product (445 nm) and DLER product (440 nm), and their differences (GE_LER-DLER)

These differences are also reflected in the probability density histograms of surface albedo for the selected study dates (Figure 3-2). For snow and ice-covered surfaces (albedo approaching 1.0), DLER exhibits a sharp peak centered near 0.95, whereas GE_LER shows a substantially broader distribution. Over the oceans, the DLER distribution is relatively narrow, with a pronounced peak between 0.025 and 0.05. In contrast, GE_LER displays a relatively broader distribution, with a considerable fraction of values extending towards very low albedos (0.0–0.025). This behavior is likely attributable to the geometry-dependent formulation of GE_LER, which explicitly accounts for variations in illumination and viewing geometry over water surfaces, whereas DLER assumes isotropic Lambertian-equivalent reflectivity

.

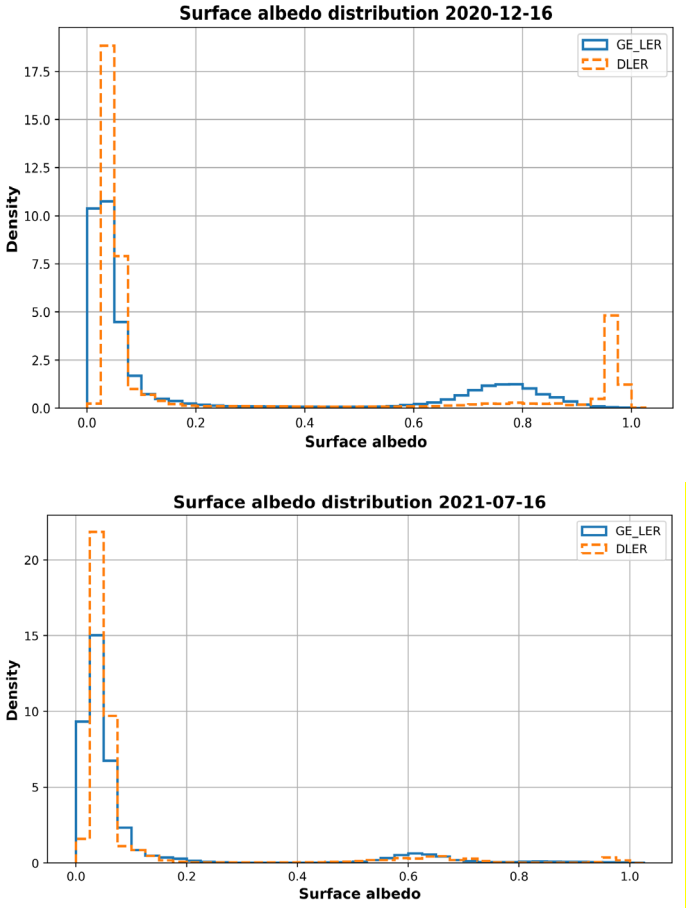


Figure 3-2: Normalised histograms of surface albedo from TROPOMI observations on 16 December 2020 (top) and 16 July 2021 (bottom), as provided by the GE_LER and DLER products at 440 nm. The histograms are normalised such that the total area under each histogram equals one.

Air mass factor calculations for the HCHO retrieval are performed at 340 nm, and DLER and GE_LER provide albedo values for this wavelength (Table 1). The comparison of DLER and GE_LER for the same orbits as Figure 3-1 is shown in Figure 3-3. Again, GE_LER is generally higher than DLER, except for some regions in the middle of the orbit. We also see smaller differences over the snow/ice regions over Antarctica for winter, while we see higher GE_LER over the North Pole in the summer. For 340 nm, over water, GE_LER is higher than DLER, in contrast to 440 nm, where DLER is higher over water.

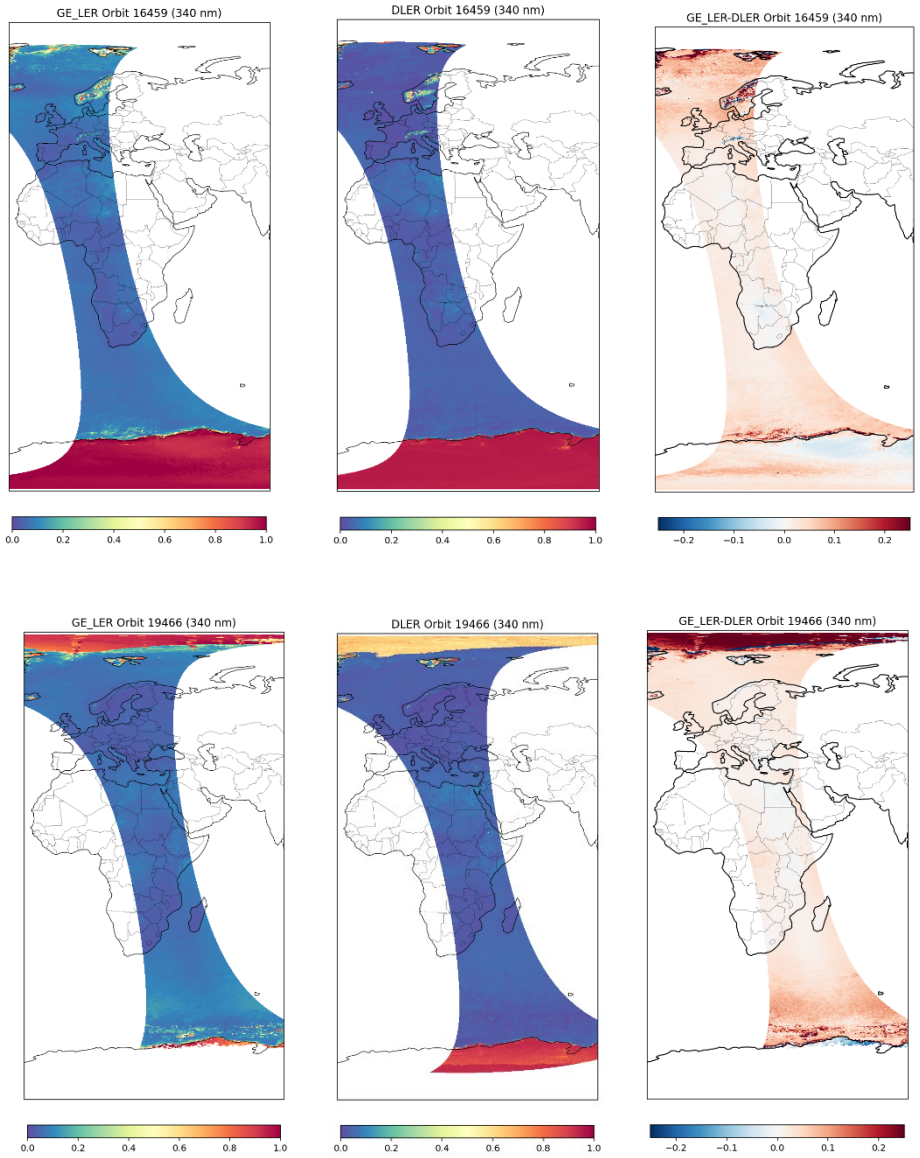


Figure 3-3: Lambertian-equivalent reflectance on 16 December 2020 for TROPOMI orbit 16459 (upper panels) and for 16 July 2021 (orbit 19466, lower panels), as predicted by the DLER product (340 nm) and GE_LER product (344 nm), and their differences.

A comparison of the surface albedo distribution for the two study days was performed. At 340 nm, DLER shows lower values than the GE_LER for surface albedo below 0.3, which corresponds to water and land pixels. Over snow/ice pixels (albedo close to 1), in December the DLER shows a narrow peak at ~0.95, while for GE_LER the snow/ice pixels show a more spread-out distribution. Unlike DLER climatologies, which are calculated at discrete single wavelengths (e.g., 340 nm for HCHO, 440 nm for NO2), GE_LER spans the continuous wavelength fitting windows used in operational trace-gas retrievals (e.g., 328–359 nm for HCHO, 435-455 nm for NO_2 and TCWV), thereby accounting for wavelength dependence. Also, GE_LER exhibits a noticeable increase in surface reflectivity in the UV relative to the visible range over snow and ice-covered surfaces. This elevated reflectivity in the UV range might be an underestimation of Rayleigh scattering or ozone

absorption during the GE_LER atmospheric correction process. In addition, differences in the post-processing gap-filling procedures between GE_LER and DLER may further contribute to these observed discrepancies.

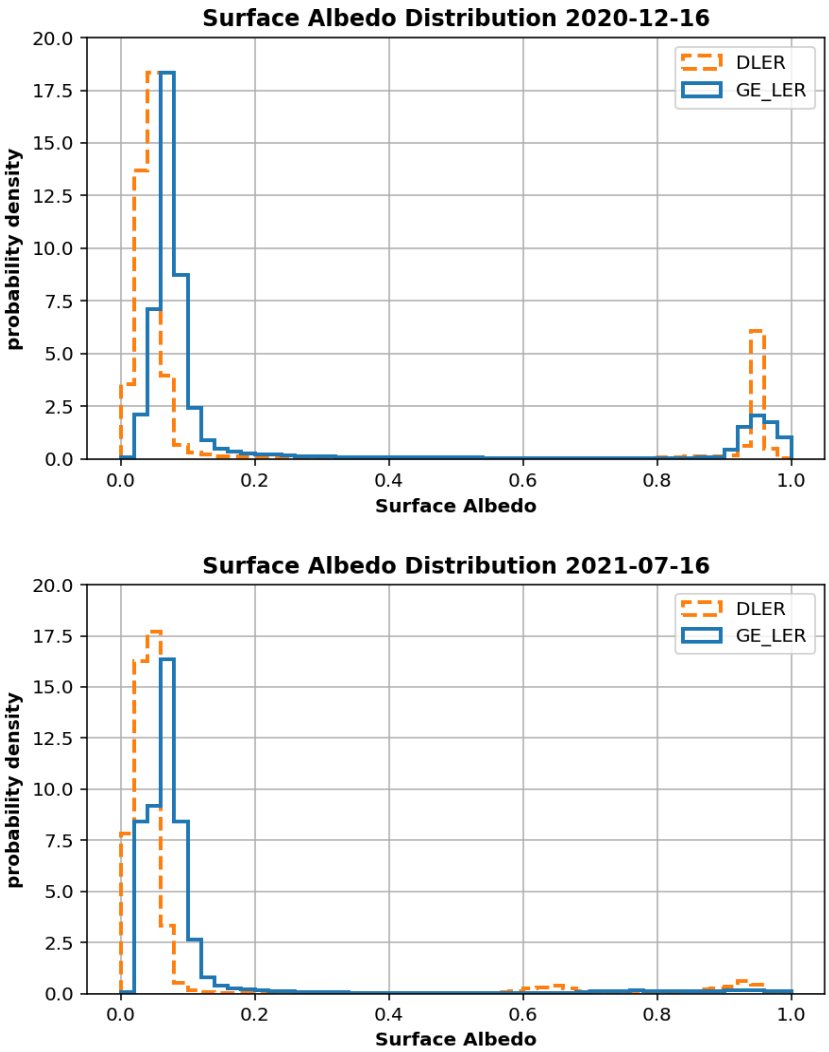


Figure 3-4: Probability density histograms of surface albedo from TROPOMI observations on 16 December 2020 (top) and 16 July 2021 (bottom), as provided by the GE_LER and DLER products at 340 nm.

To further evaluate the performance of the two datasets over dark vegetated surfaces, the Amazon Basin was investigated in December (austral summer). This region provides an excellent test case because it is covered by dense evergreen rainforest, representing one of the darkest natural surfaces in the UV–visible spectral range, while also experiencing high solar elevation angles. These characteristics make the region particularly suitable for evaluating a geometry-dependent surface reflectance product.

As shown in Figure 3-5, GE_LER and DLER reproduce similar surface albedo ranges and spatial structures across the Amazon Basin, with differences generally remaining within ±0.05. Both datasets indicate slightly higher surface reflectance over the eastern part of the orbit, consistent with changes in illumination and viewing geometry across the satellite swath. In addition, GE_LER

produces a sharper land–ocean transition and a relatively stronger reflectance contrast between the rainforest and the adjacent Atlantic Ocean than DLER.

It should be noted that the GE_LER climatology is currently in a beta stage and remains under active development. Ongoing refinements aim to reduce these discrepancies and improve the overall consistency and robustness of the product.

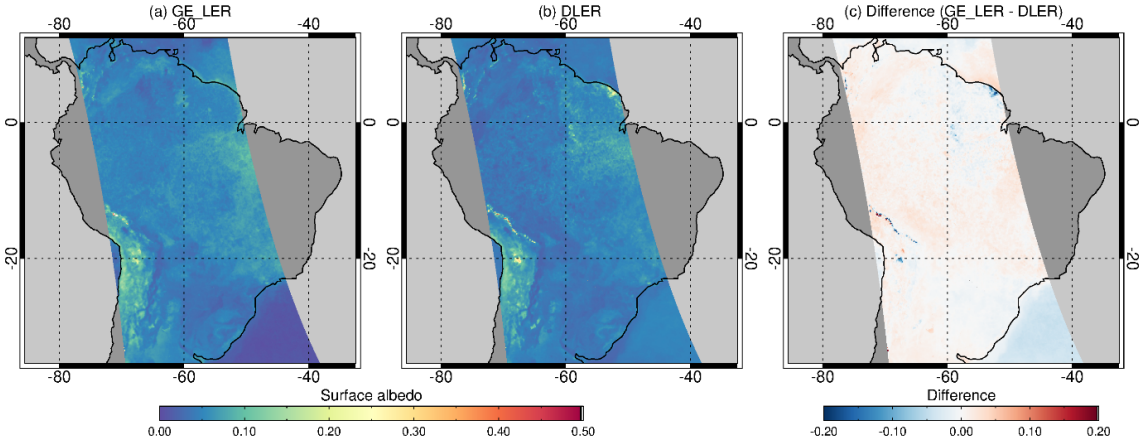


Figure 3-5: Zoomed-in maps of surface reflectance over the Amazon Basin for TROPOMI orbit 16462 on 16 December 2020, derived from the DLER product (440 nm) and the GE_LER product (445 nm), and the corresponding differences between the two datasets.

3.1.4 Spatial resolution

To verify the spatial resolution of two directional surface reflectivity databases that both claim to be 0.125°, we used a combination of metadata inspection, visual analysis, and quantitative checks.

Figure 3-6 shows the DLER and GE_LER albedo climatologies for November and their difference. To assess whether the spatial resolution of 0.125° is representative of the surface, we select a region with long coastlines and a large contrast between sea and land, where over the Sahara albedo is high, while over the sea albedo is low. From a visual analysis, we see that both databases resolve coastlines well.

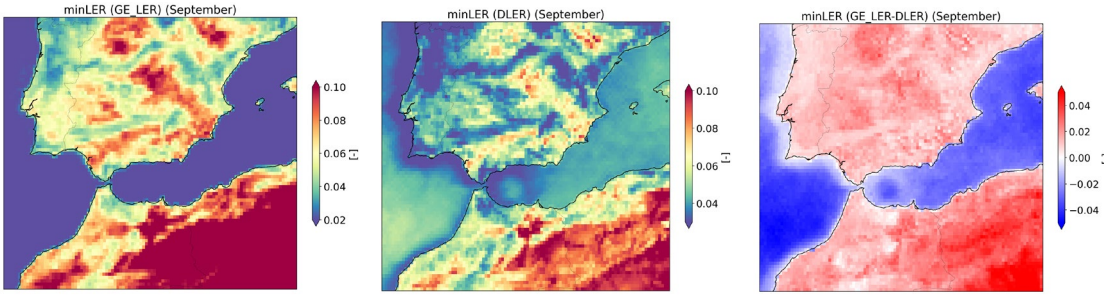


Figure 3-6: (a) Minimum LER from the GE_LER database, (b) minimum LER from the DLER database, (c) difference between GE_LER and DLER. Both minimum LERs are selected for the month of November at 440 nm (DLER) and at 435-355 nm (GE_LER) for the strait of Gibraltar, parts of Spain, Morocco, and the western Mediterranean.

3.1.5 Temporal representativeness

Figure 3-7 shows the temporal variability of the surface albedo value at 440 nm for an agricultural area in the Po Valley derived from the S5P DLER, the OMI LER, and the S5P minLER from the DLER and GE_LER databases. As expected, we see that the DLER is higher than the KNMI minLER, due to the increase in reflectivity when accounting for viewing angle dependency, which changes from day to day. Moreover, we see that OMI LER is higher than the TROPOMI minLER, often close to the DLER values. OMI LER climatology (0.5°x0.5°) uses the modeLER, and not the minLER,and is also coarser than the S5P LER climatology (0.125°x0.125°), and both are constructed using the first few years of level-1 data from the OMI and TROPOMI instruments, respectively, which can explain the discrepancies between the two datasets. Moreover, the minLER from the GE_LER database is consistently higher than the minLER from the DLER database, but they show similar temporal fluctuations.

Regarding the seasonality of the albedo, we observe peaks around April and around October, and two dips, one in winter and one in July-August. This is likely caused by variations in chlorophyll absorption, surface properties (due to local agricultural practices), and the solar zenith angle. Chlorophyll absorbs at 430-450 nm, which can interfere with the 440 nm wavelength band, and chlorophyll absorption can be strong during summer, resulting in decreased surface albedo. During autumn, harvest usually takes place, exposing the soil, which reflects more blue light. The behavior of the albedo is similar to what is shown in Figure 5 of Starr et al. (2020), where the MODIS black-sky cropland albedo in the blue channel (470 nm) for different types of crops reduces during the summer and is high during spring and autumn. The reduced albedo during winter might be partially explained by the lower solar zenith angle.

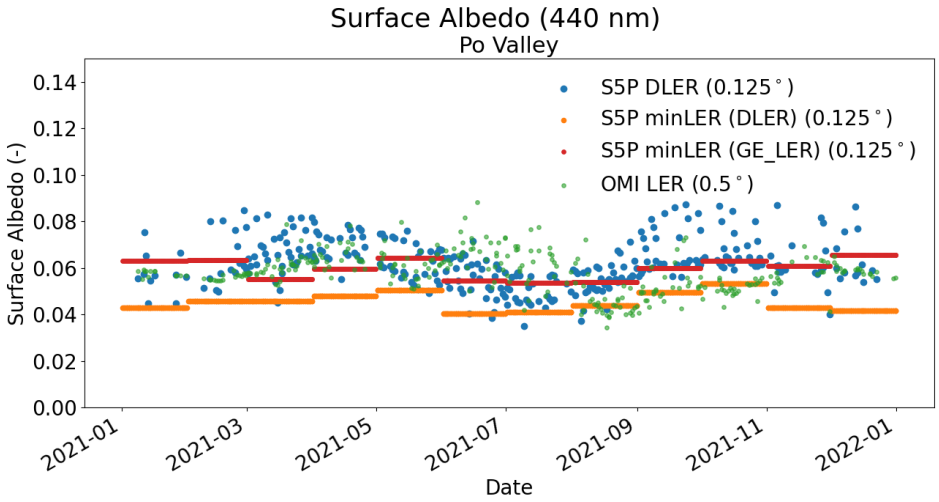


Figure 3-7: Temporal variability in surface albedo derived on orbit basis from the S5P DLER and the OMI LER, spatially averaged at 0.2° resolution, and the monthly S5P minLER of the DLER database (v2.2 at 440 nm), and from the GE_LER database for H2O (v3.3.1, 435-455 nm) , for an agricultural area in the Po Valley (45.3°N, 9.7°E). The spatial resolution of the S5P DLER and minLER climatologies are 0.125°x0.125° and the resolution of the OMI climatology is 0.5°x0.5°. The DLER shown in the figure is consistent with TROPOMI NO2 v2.4 retrieval, which is based on the S5P minLER v1.0 climatology (from the DLER database, 3 years of TROPOMI data), while the figure shows the DLER minLER v2.2 (7 years of TROPOMI data), but we do not expect significant variation between the two versions.

3.1.6 Directionality

Figure 3-8 below shows a comparison of the DLER and GE_LER values at 440 nm as a function of TROPOMI viewing zenith angle over the Amazon region and Europe in December 2020 and July 2021. As expected, the directional surface reflectivity is highest for the most extreme viewing zenith angles in both DLER and GE_LER. The minLER of the GE_LER database is higher than the minLER of the DLER database for both regions. The surface albedo appears higher in the east than in the west part of the orbit because the sun is behind the sensor (relative to the surface), leading to more direct illumination of the surface and higher reflectance. In the west, the Earth's surface appears darker because natural surfaces like vegetation forward-scatter light, leading to lower reflectance when viewed from the sensor (negative VZA). For the east part of the orbit, we see better agreement between the two datasets, while in the west part, DLER mostly stays close to the minLER values, but GE_LER decreases until angles around -40°, and increases again for more extreme angles.

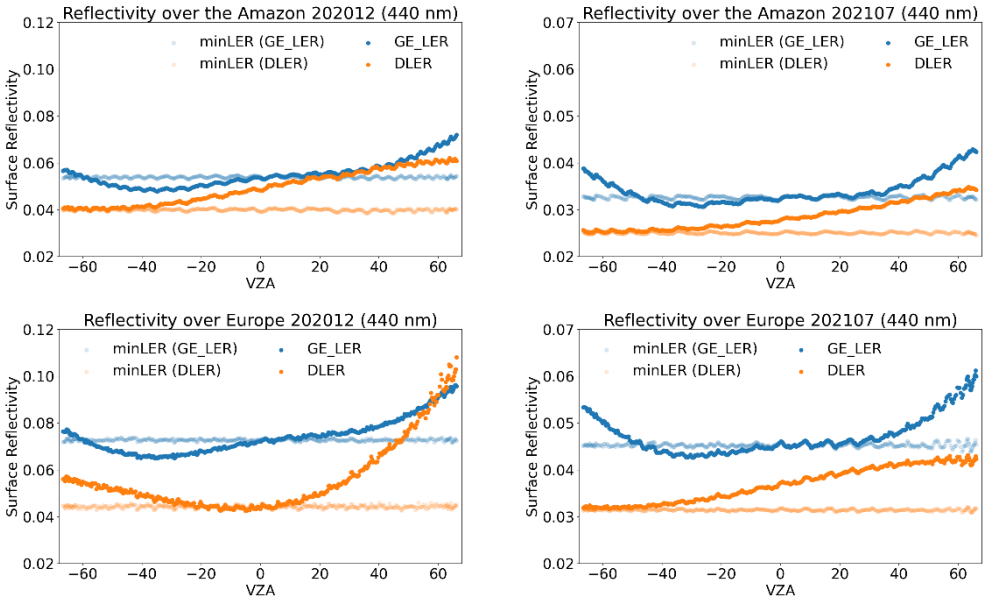


Figure 3-8: Surface reflectivity values at 440 nm as a function of TROPOMI viewing zenith angle over the Amazon (0°-10°S, 55°E – 65°E) and Europe (4°E- 17°E, 47°N-55°N, excluding water pixels) from the DLER (blue) and GE_LER (orange) databases for December 2020 and July 2021. For comparison, the MINLER values of each database are also shown (in lighter blue and orange).

In Figure 3-9 we compare the differences between the DLER and the GE_LER for these regions for the same months, and the distribution of the differences shows that GE_LER is higher than DLER, with a median difference ranging from 0.005 to 0.02. For July we see a small spread of the differences, while for December we see a larger spread, and as seen in the lower panels of Figure 3-8 for Europe, DLER at the eastern edges of the orbit shows higher values than GE_LER.

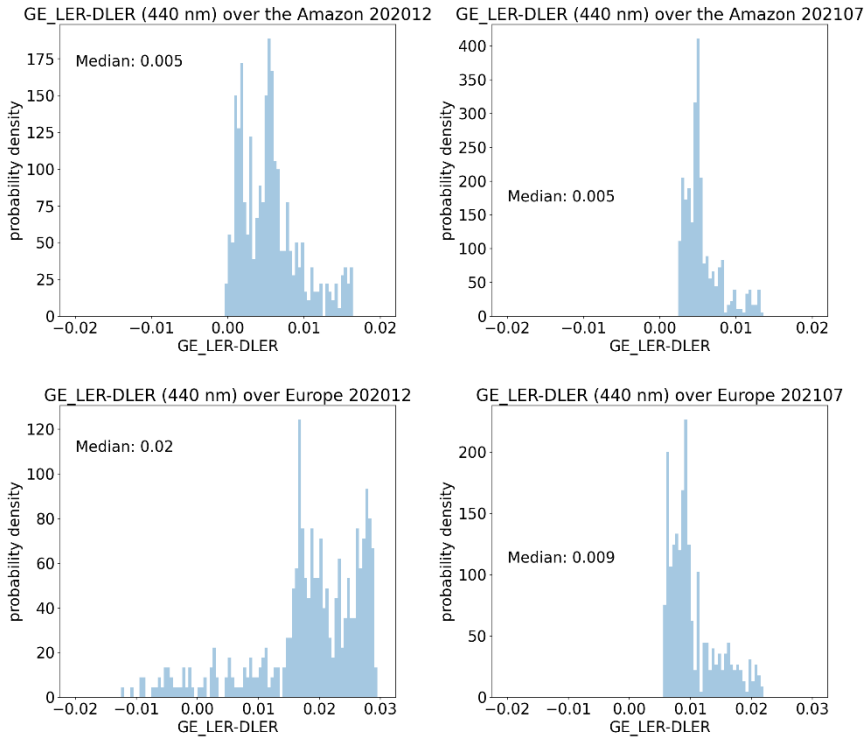


Figure 3-9: Probability density function of DLER and GE_LER differences for December 2020 and July 2021 over the Amazon (0°-10°S, 55°E – 65°E) and Europe (4°E- 17°E, 47°N-55°N, excluding water pixels) for 440 nm

The analysis of Figure 3-8 and Figure 3-9 suggests that the DLER and GE_LER databases capture the viewing zenith angle (VZA) dependency of surface albedo, at least around 440 nm. Both datasets show the expected anisotropic behavior: higher reflectance in the east (sun behind the sensor) and lower in the west (forward-scattering by vegetation). However, DLER maintains a smoother relationship with VZA, especially in the west, where GE_LER exhibits unexpected decreases at moderate negative viewing zenith angles (-40°) and increases at more extreme angles.

A similar comparison of the two datasets over the same regions and months is performed at 340 nm, yielding results similar to those for the 440 nm range (Figure 3-10 below). The minLER from the GE_LER database is higher than the one from the DLER database, which also results in higher GE_LER. Moreover, DLER shows increasing albedo values relative to the minLER in the eastern part of the orbit, as expected from anisotropic scattering theory (e.g. Lorente et al., 2018). GE_LER shows small increases on the left side as well.

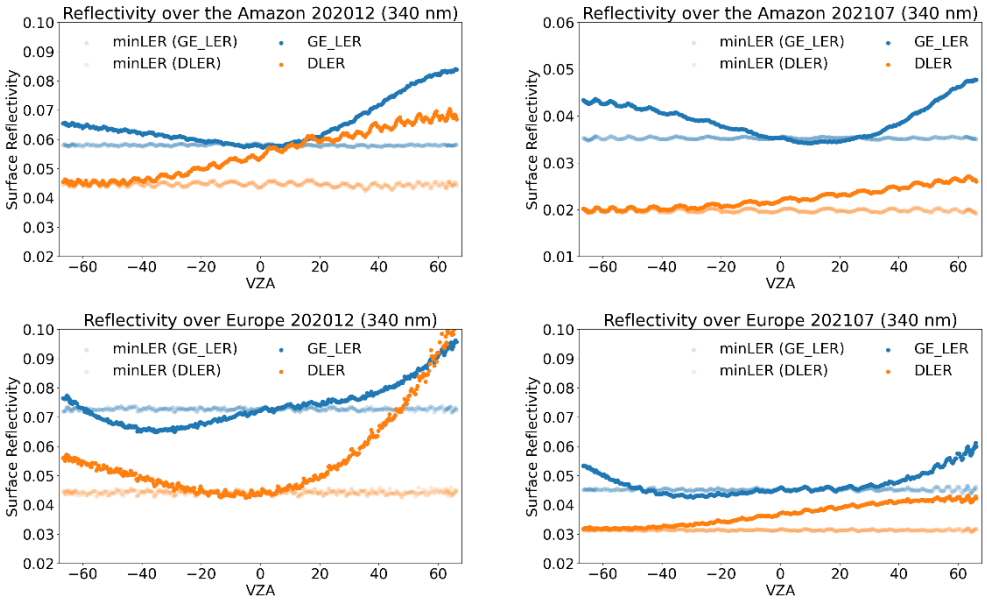


Figure 3-10: Surface reflectivity values at 340 nm as a function of TROPOMI viewing zenith angle over the Amazon (0-10°S, 55°E – 65°E) and Europe (4°E- 17°E, 47°N-55°N, excluding water pixels) from the DLER (blue) and GE_LER (orange) databases for December 2020 and July 2021. For comparison, the minLER values of each database are also shown (in lighter blue and orange).

Figure 3-11 shows the distribution of the differences of the 340 nm surface reflectivity values between DLER and GE_LER. The median difference in surface reflectivity ranges from 0.01 to 0.02, with DLER lower than GE_LER. These differences are somewhat larger than found for 440 nm, indicating stronger uncertainty in surface reflectivity for HCHO than for NO_2.

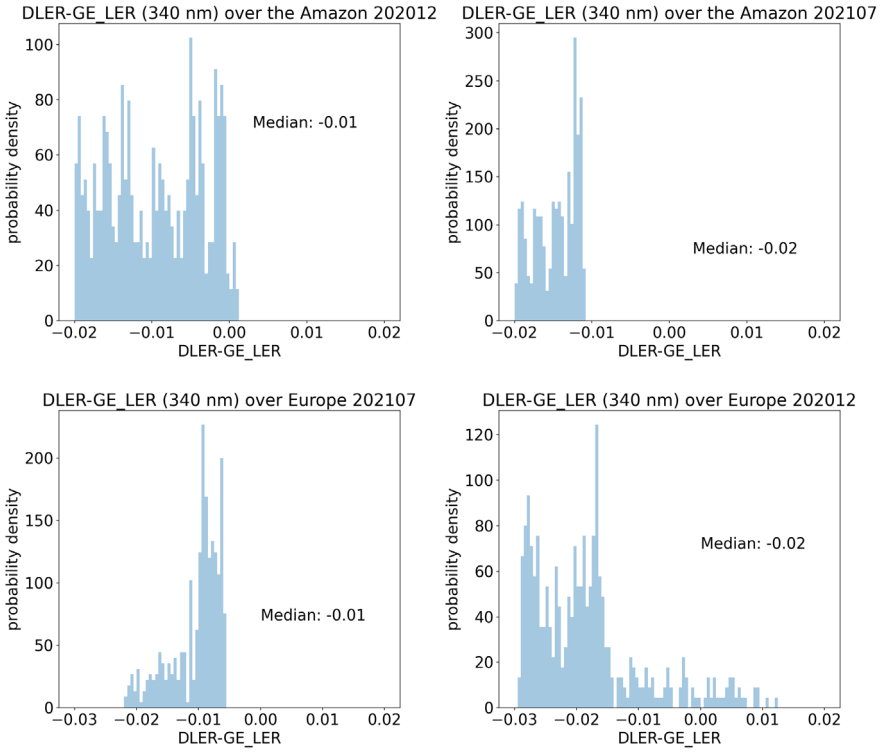


Figure 3-11: Probability density function of DLER and GE_LER differences for December 2020 and July 2021 over the Amazon (0°-10°S, 55°E – 65°E) and Europe (4°E- 17°E, 47°N-55°N, excluding water pixels) for 340 nm.

3.2 Impact of directional reflectance on cloud parameters

The KNMI TROPOMI NO_2 retrieval uses the cloud pressure obtained from the FRESCO retrieval at 758 nm. The cloud (radiance) fraction used for the NO_2 product is retrieved at 440 nm. The surface reflectivity is generally more sensitive to the viewing angle dependency at 758 nm than at 440 nm (e.g. Lorente et al., 2018). This is visualised in Figure 3-12, where the albedo, cloud fractions, and cloud pressures are shown for two different versions of the TROPOMI NO_2 product, v2.3.1 with albedo from TROPOMI minLER (no directionality), and v2.4 with albedo from DLER (directionality included).

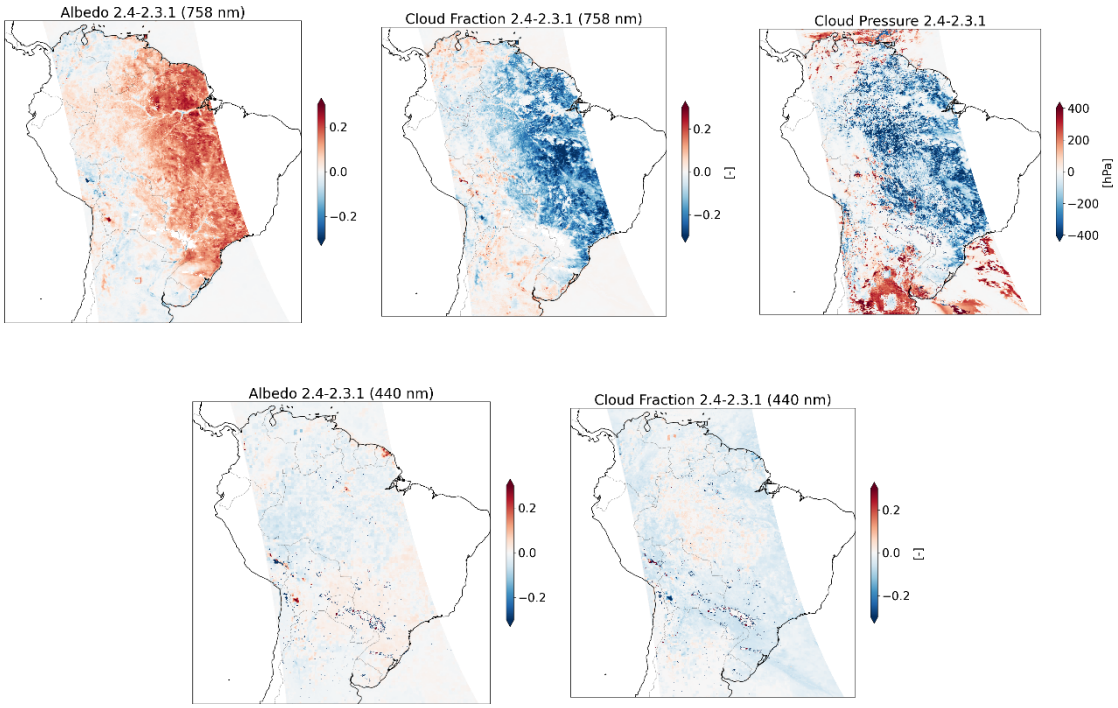


Figure 3-12: Surface albedo, cloud fraction and cloud pressure at 758 nm, and surface albedo and cloud fraction at 440 nm comparison between TROPOMI NO_2 product v2.4 and v2.3.1 over South America on 16 December 2020 (Orbit 16462).

The upper left panel of Figure 3-12 shows the differences between DLER and MINLER surface reflectivities when sampled over real viewing geometries in a particular TROPOMI orbit (on 16 December 2020) over South America. At 758 nm, the surface reflectivities differ strongly at the east side of the orbit, as expected. The corresponding differences in cloud fraction and cloud pressure retrieved with FRESCO using the DLER and MINLER as inputs are consistent with the higher surface reflectivities in the east: the radiance closure in FRESCO imposes that higher assumed surface reflectivities are compensated by lower cloud fractions. The lower two panels show that surface reflectivity differences between DLER and MINLER are much smaller at 440 nm, and that the corresponding cloud fraction differences (at 440 nm) are less pronounced than at 758 nm.

3.3 Impact of directional reflectance on NO_2 retrievals

The NO_2 Air Mass Factor (AMF) calculations depend on the surface albedo and the cloud pressure for partly cloudy pixels via the independent pixel approximation used in the AMF calculation:

$$M_{trop} = \frac{(1-f_{cl})R_{clear}M_{clear}+f_{cl}R_{cloud}M_{cloud}}{R_{sat}} \quad (3)$$

Where M_{clear} and M_{cloud} represent the NO_2 air mass factors calculated for a completely clear-sky and cloudy situation, respectively, and f_{cl} is the retrieved cloud fraction for the pixel, and R_{clear} and R_{cloud} are the clear-sky and cloudy-sky radiances, which divided by R_{sat} (R_{sat} =

$(1 - f_{cl})R_{clear} + f_{cl}R_{cloud})$ give the clear-sky and cloudy-sky reflectance weights. The clear and cloud-sky radiances are calculated at 437.5 nm using the rweight routine from the DOMINO codebase as a theoretical estimate of the Rayleigh scattering + surface reflection contributions to the top-of-atmosphere radiance:

$$R = R_{Rayleigh} + T_{\mu_0} T_{\mu} \frac{A_{sfc}}{1 - A_{sph} A_{sfc}} \quad (4)$$

where $R_{Rayleigh}$is obtained from the Chandrasekhar-type polynomial approximation, A_{sfc} is the surface (or cloud) albedo, and A_{sph} is the spherical albedo of the atmosphere (0.1 for clear-sky and 0.5 for the cloudy atmosphere).

From Eq. (3) and Eq. (4) it is apparent that changes in cloud parameters and surface albedo will impact the clear-sky and cloudy AMFs, as well as the reflectance weights between the clear-sky and cloudy parts of a pixel. Both the cloud fraction and the cloud pressure change when using the DLER as indicated by the rightmost panels of Figure 3-12. An increase in the surface albedo due to using DLER is expected to result in decreases in the cloud fraction and the cloud pressure. Decreases in cloud fraction can result in increases in NO_2, while decreases in cloud pressure,due to a decrease in the light path, would result in lower tropospheric AMF values, because clouds that are situated higher in the atmosphere cause more screening of NO_2 below.

Figure 3-13 shows the differences in the NO_2 AMFs and the tropospheric vertical columns for the same orbit as Figure 3-12. It is obvious that especially the decreased cloud pressures have led to lower AMFs, which results in increases in the NO_2 columns. For the area shown in the figure, the mean increase of the NO_2 column is 6.8 % and the mean decrease of the AMF is 4.3%. For a smaller box containing only the Amazon forest (12°S-2°N, 50°W-70°W) the mean increase of the NO_2 column is 11.6 % and the mean decrease of the AMF is 7.8%).

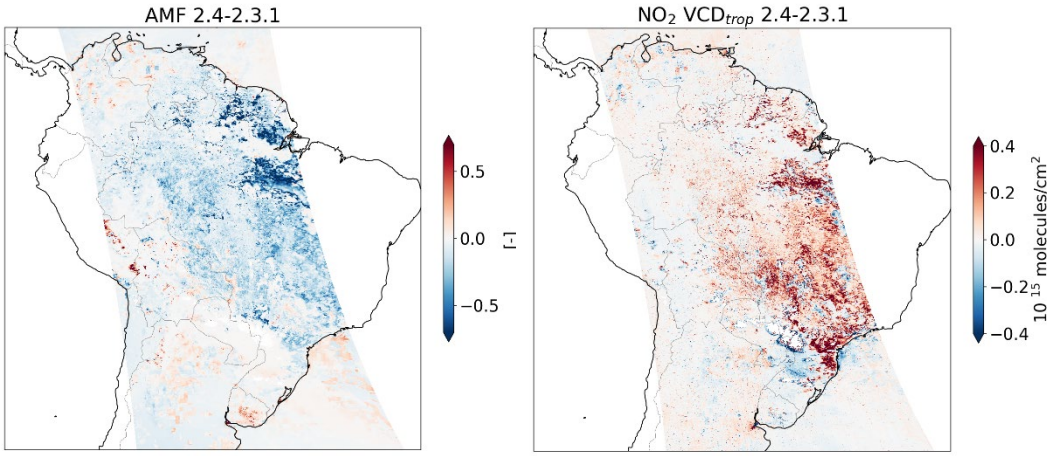


Figure 3-13: NO_2 AMF and tropospheric column differences between TROPOMI NO_2 product v2.4 and v2.3.1 over South America on 16 December 2020 (Orbit 16462).

3.4 Impact of directional reflectance on HCHO retrievals

The TROPOMI HCHO retrieval is performed at 340 nm. We use a test dataset where the HCHO column is retrieved using different surface reflectivity databases, namely, a retrieval using the TROPOMI DLER, and one using the TROPOMI minLER, similar to what is shown above for NO_2. This test dataset was created during the CCI round robin exercise, and unfortunately the GE_LER database was not available at that time. For this test dataset, the only variable changing is the surface albedo input in the AMF calculation, which proceeds differently compared to NO_2. In the HCHO retrieval, no independent pixel approximation is applied, and retrievals are considered valid only when cloud fractions (from the OCRA-ROCINN cloud retrieval) are below the threshold value of 0.4. The only difference between the TROPOMI DLER and minLER retrievals is then from the clear-sky AMF values calculated for different surface albedo datasets. Generally, clear-sky HCHO AMFs are higher for higher surface albedo values (e.g. De Smedt et al. (2018); Lorente et al. (2017)).

The left panel of Figure 3-14 shows that DLER surface albedo values are higher (especially at the eastern part of the orbit) than minLER values, in line with the results shown in Figure 3-10. The center panel shows that the corresponding AMF values increase by up to 0.15 over South America on 15 January 2020, consistent with findings in previous research. In turn, the higher AMF values result in lower tropospheric HCHO columns over South America (right panel of Figure 3-10), with differences of -0.1 10^{15} molec.cm^{-2} in the domain. These differences are only small, -0.5% on average. This limited impact is expected because HCHO retrievals have relatively low sensitivity to the boundary layer, where the main changes in photon path length by surface albedo occur, while Rayleigh scattering dominates the radiative transfer at the retrieval wavelengths (Lorente et al., 2017). Consequently, changes in surface albedo have a much smaller influence on the HCHO AMF than on trace gases such as NO_2, whose retrievals exhibit greater boundary-layer sensitivity.

For the above reasons, HCHO retrievals generally use minLER at 340 nm. The CCIp HCHO product version 2 uses minLER from the DLER climatology, while minLER from the GE_LER climatology has been recently introduced in the latest version of the operational TROPOMI HCHO product (previously minLER from the OMI climatology). Systematic differences in minLER across the different climatologies, as shown in Figure 3-10, will result in systematic uncertainty of the HCHO VCD of (less than 10% on average, see section 3.4.1 of the Precursors_cci+_D2.3_PVASR_01_01).

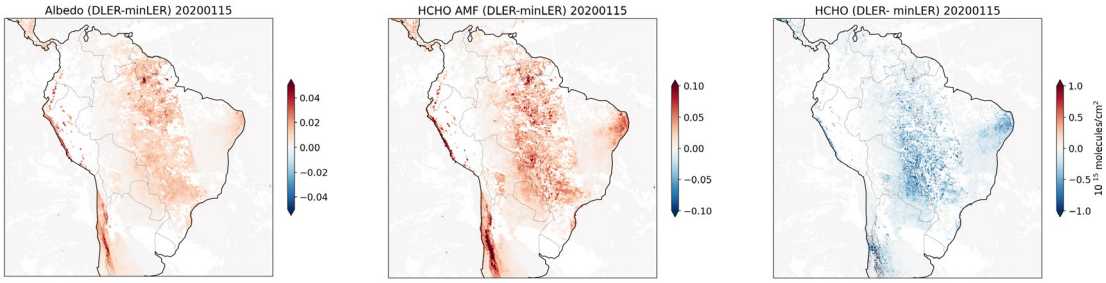


Figure 3-14: Surface albedo (340nm), HCHO AMF and tropospheric column comparison between test daily HCHO columns using DLER and minLER for the retrieval over South America on 15 January 2020.

3.5 Validation

3.5.1 Clouds

3.5.1.1 OCRA ROCINN upgrade from version 1 to version 2

The S5P OCRA/ROCINN CLOUD OFFL processor version switched from UPAS version 1 to UPAS version 2 at measurement date 2020/07/17. In this version change, the MERIS albedo was replaced by the GE_LER albedo. Note, however, that other algorithm changes were also introduced at this point (see ATM-MPC L2_CLOUD Product Readme File (PRF-CLOUD) by R. Lutz et al., 2025). Both versions were validated within the ATM-MPC using another satellite cloud product (S5P FRESCO-S) and ground-based Cloudnet data, and the results presented here are based on these studies. Two variants of S5P OCRA/ROCINN product exist: ROCINN_CAL ("Clouds as layers", with a finite thickness) and ROCINN_CRB ("Clouds as reflecting boundaries"), and both are considered here. The validation methodology is based on (Compernolle et al., 2021) updated within the ATM-MPC operational validation (e.g., ROCVR#17 (Lambert et al., 2022)).

Comparison of the OCRA/ROCINN_CAL cloud top height (CTH) product with S5P FRESCO-S cloud height (CH) over Cloudnet sites reveals that the cloud height difference dispersion between the two products is strongly reduced upon the UPAS version switch (Figure 3-15, top, taken from ROCVR#17 (Lambert et al., 2022)). The dispersion reduction is seen at most sites, but especially above high-latitude sites (e.g., Ny-Ålesund) in winter time (e.g., Norunda), suggesting that snow-ice is an important factor. Note that the FRESCO-S product was not changed on this date.

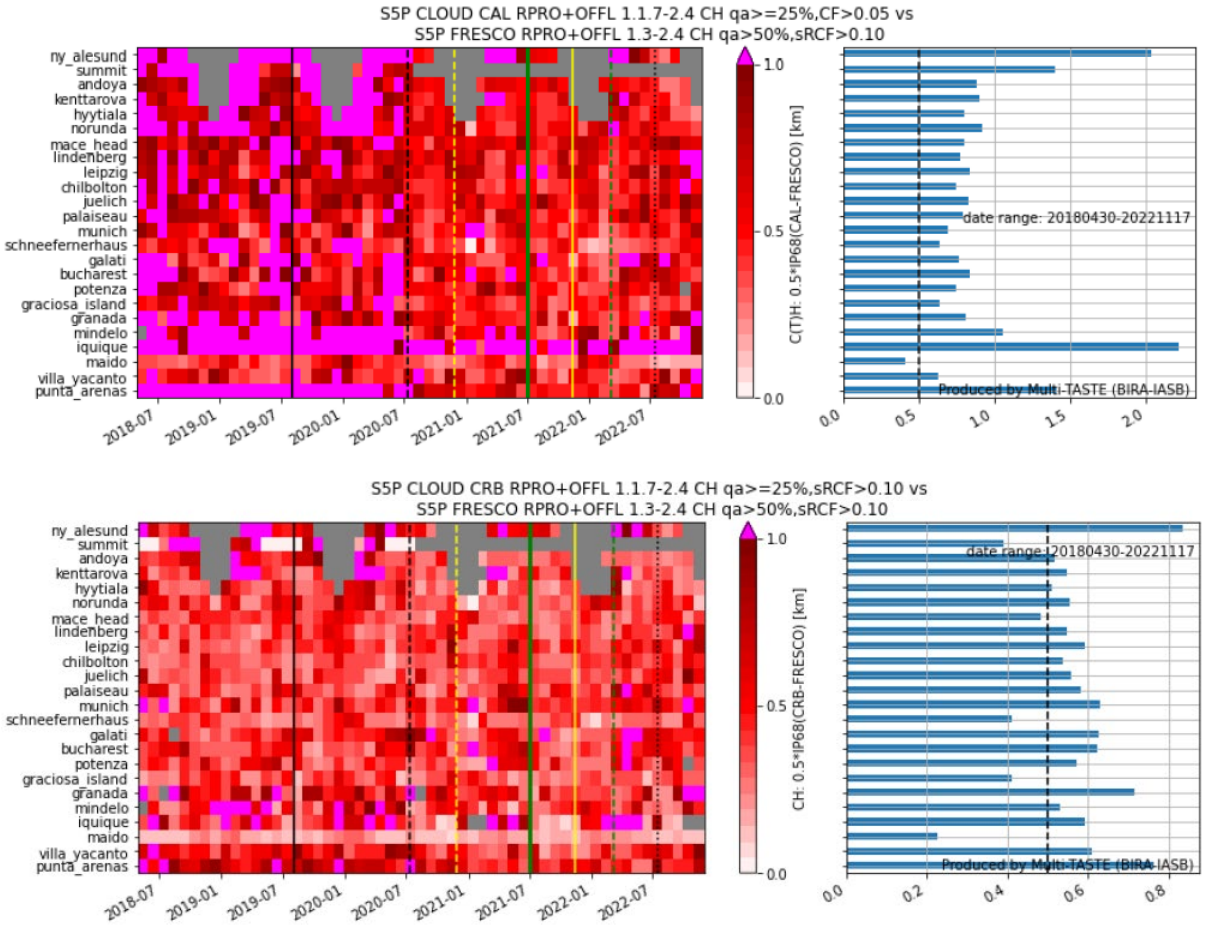


Figure 3-15. Top. Left. Monthly dispersion (1/2 IP68) of CLOUD ROCINN_CAL CTH minus FRESCO CH, per station. The version upgrade from UPAS v1 to UPAS v2 on 2020/07/13 is indicated by a black dashed line. Right. Dispersion over the full time range. Figure taken from ROCVR#17 (Lambert et al., 2022). Bottom: same but for CLOUD ROCINN_CRB CH minus FRESCO CH.

Table 3-2 presents validation results of OCRA/ROCINN_CAL v1 and v2 CTH with respect to ground-based ACTRIS-CLOUDNET CTH. Noticeable is a decrease in dispersion for high and low clouds (e.g., from 0.8 km to 0.6 km for low clouds), and a clear improvement in correlation.

Table 3-2. Validation statistics of S5P CLOUD OCRA/ROCINN_CAL cloud top height (CTH) versus ACTRIS Cloudnet CTH. To obtain the overall bias and dispersion, first the QI is calculated per station (median difference, median relative difference and ½ of the central 68-interpercentile of the difference), then the median over all stations is taken. Table adapted from ROCVR#17, Table 19 (Lambert et al., 2022). The distinction between low and high clouds is taken at Cloudnet CTH=4 km.

CAL CTH-CLOUDNET CTH	#sites	Bias: Med(meddiff)	Rel bias: Med(medreldiff)	Dispersion: Med(1/2IP68)	Pearson R
CLOUD v1; high	21	-2 km	-33%	2.2 km	0.38
CLOUD v1; low	21	-0.3 km	-12%	0.8 km	0.32
CLOUD v2.1; high	12	-3 km	-41%	1.9 km	0.51
CLOUD v2.1; low	12	-0.3 km	-14%	0.6 km	0.52

CLOUD ≥v2.2, high	16	-3 km	-38%	1.9 km	0.52
CLOUD ≥v2.2, low	15	-0.3 km	-12%	0.6 km	0.61

A more modest reduction in cloud height dispersion is observed for OCRA/ROCINN_CRB CH versus FRESCO CH over several sites (e.g., Granada, Iquique, Mindelo, ...: see Figure 3-15, bottom).

Table 3-3 presents validation results of S5P CLOUD OCRA/ROCINN_CRB cloud height with respect to ACTRIS Cloudnet cloud mean height. There is a modest reduction of the dispersion for low clouds (from 0.6 km to 0.5 km), and a clear improvement in correlation for low clouds.

Table 3-3. Validation statistics of S5P CLOUD OCRA/ROCINN_CRB cloud height (CH) versus ACTRIS Cloudnet cloud mean height (CMH). To obtain the overall bias and dispersion, first the QI is calculated per station (median difference, median relative difference and ½ of the central 68-interpercentile of the difference), then the median over all stations is taken. Table adapted from ROCVR#17, Table 19 (Lambert et al., 2022). The distinction between low and high clouds is taken at Cloudnet CTH=4 km.

CH: CRB CH- CLOUDNET CMH	#sites	Bias: Med(meddiff)	Rel bias: Med(medreldiff)	Dispersion: Med(1/2IP68)	Pearson R
CLOUD v1; high	21	-0.9 km	-20%	1.6 km	0.47
CLOUD v1; low	21	-0.5km	-36%	0.6 km	0.19
CLOUD v2.1; high	12	-1.2 km	-25%	1.8 km	0.43
CLOUD v2.1; low	12	-0.6 km	-40%	0.4 km	0.52
CLOUD ≥v2.2, high	16	-1.4 km	-27%	1.8 km	0.48
CLOUD ≥v2.2, low	15	-0.7 km	-40%	0.5 km	0.46

In conclusion, comparing OCRA/ROCINN v1 with v2, a clear reduction in dispersion is seen for ROCINN_CAL and a more modest one for ROCINN_CRB, while the correlation improves for both products. However, apart from the albedo change from MERIS to GE_LER under investigation, several other important algorithmic changes were introduced with v2 (e.g., new cloud free maps, based on TROPOMI instead of OMI; and an updated filtering scheme), which could also contribute to this improvement.

3.5.1.2 S5P FRESCO-S upgrade from version 2.2-2.3 to version 2.4

The operational S5P FRESCO-S product switched from version 2.3 to 2.4 on 2022-07-16. The GOME-2-based minLER surface albedo was replaced with an S5P-based DLER at this point; no other important FRESCO updates were introduced at that time. Note that the S5P NO2 product switched from an OMI based minLER to an S5P-based DLER at the same time (see ATM-MPC L2_NO2 Product Readme File (PRF-NO2) by Eskes et al., 2025).

We investigated the impact on the retrieved cloud height by comparing the two versions with ACTRIS Cloudnet. Both data versions were validated within the ATM-MPC. We collected here the collocated data sets of both versions for a delta-validation:

- S5P FRESCO-S OFFL 2.2-2.3, covering the period 2021-07-1 to 2022-07-16. Note that there was no algorithmic update between 2.2 and 2.3 for FRESCO, so there is no problem in taking both together. Older (1.4 and lower) and newer (2.4 and higher) versions are excluded here because of major differences.
- The reprocessed dataset S5P FRESCO-S RPRO 2.4. For the present delta-validation work, we took only the period 2021-07-1 to 2022-07-16.

For both datasets, FRESCO cloud height was compared to Cloudnet cloud mean height. Figure 3-16 presents correlation plots and statistics for both.

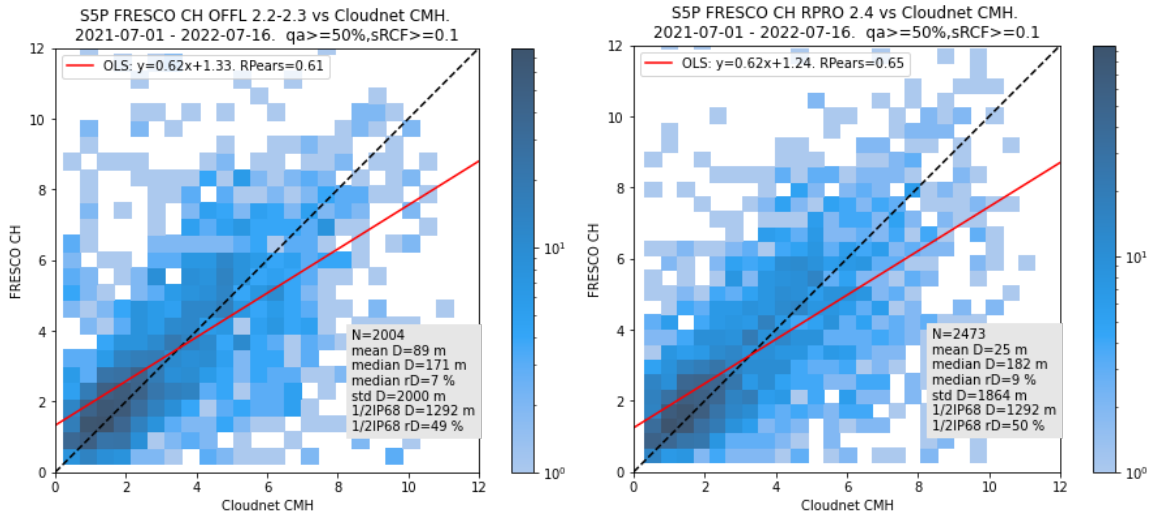


Figure 3-16 Comparison of S5P FRESCO-S cloud height with ACTRIS Cloudnet Cloud mean height. Left: FRESCO OFFL v2.2-2.3. Right: FRESCO RPRO v2.4. The temporal range is 2021-07-01 to 2022-07-17, when OFFL v2.2-2.3 was active. Selected sites are Hyytiala, Norunda, Lindenberg, Chilbolton, Juelich, Palaiseau, Munich, Bucharest, Granada.

Bias, regression slope and robust dispersion (1/2IP68) are very comparable for both FRESCO versions. The correlation and the non-robust dispersion (standard deviation) are slightly better for the newest version v2.4.

In conclusion, the main improvement with the introduction of the DLER for FRESCO is a reduction in non-robust dispersion, which is an indicator of fewer outliers in the newer version.

3.5.2 NO_2

As a ground-based sanity check, two (pseudo-) operational S5P total NO_2 products can be compared to ground-based reference measurements to assess the impact of the algorithm changes: the PAL v2.3.1 reprocessing (mission start to end of 2021) used the OMI-based minLER surface model and the cloud product FRESCO v2.3, itself based on a GOME-2 minLER surface model, while the official full mission reprocessing with processor v2.4 integrated the S5P-based DLER surface model and the FRESCO v2.4, which also uses a S5P-based DLER surface model. Both data sets have previously been validated using Pandonia Global Network (PGN) direct-sun total NO_2 column data within the ATM-MPC following the approach detailed in Verhoelst et al., 2021, and the results presented here are based on those co-located data sets, harmonized for a maximal common time period and station list. Specifically, comparisons are available at 35 sites with a total of more than 10k co-locations. The co-locations are not entirely identical for both data sets, owing to both differences in quality filtering (based on the qa_value) and in availability of the

ground-based data at the time of the analyses (the PAL validation predates the v2.4 validation by about a year).

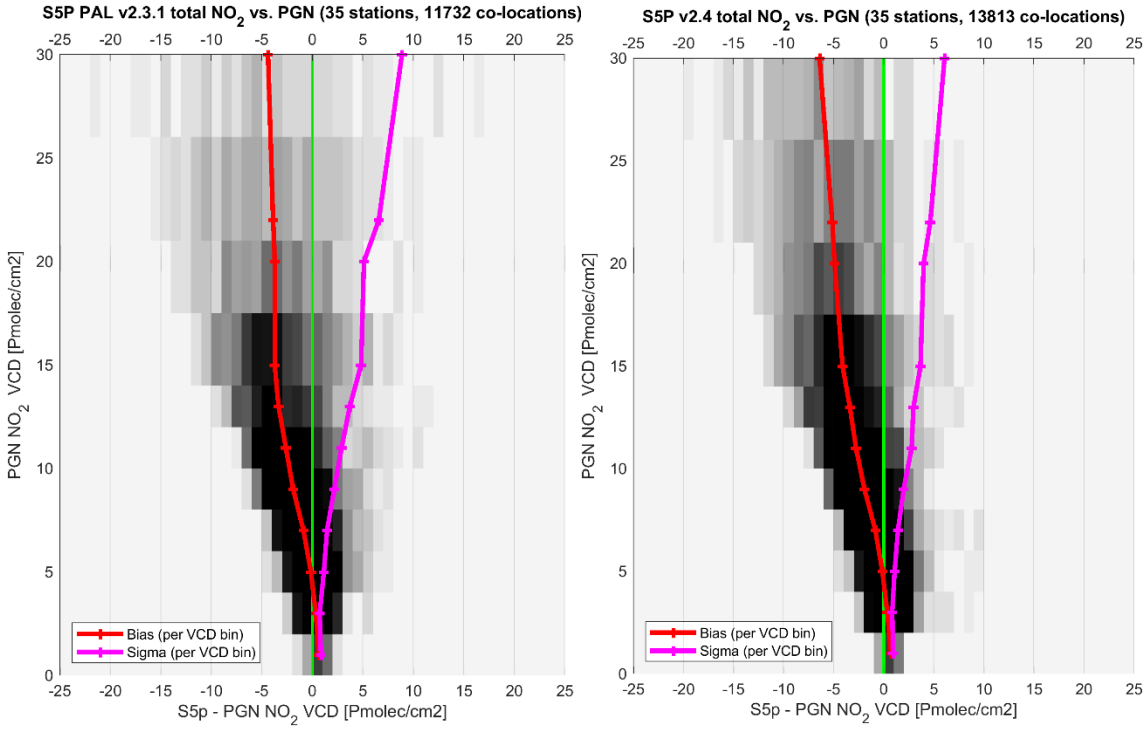


Figure 3-17: Data density (as grey scale) of the differences between S5P and PGN total NO_2 as a function of PGN total NO_2 (on the vertical axis) for the PAL v2.3.1 data (left-hand panel) and the v2.4 data (right-hand panel). Estimated bias (mean difference) and dispersion (standard deviation) per VCD bin are indicated in red and magenta, respectively. Results are roughly identical up to ~13 Pmolec/cm², above which v2.4 demonstrates a slightly more negative bias, albeit with a clearly reduced dispersion.

Figure 3-17 reveals mostly identical behaviour at low to intermediate NO_2 columns, but at higher columns, the v2.4 data show a more confined range of differences, yielding a smaller derived dispersion. The bias at these higher columns is slightly more pronounced for v2.4 though: -7 Pmolec/cm² (~23%) vs. -5Pmolec/cm² (~17%).

These differences are well detectable in the time series of the comparisons at City College in New York (Figure 3-18): while correlation coefficients are identical and the actual dispersion of the relative differences is smaller in v2.4, the underestimation is more pronounced (both as mean relative bias and – equivalently - as slope in a linear regression between satellite and ground-based columns, see Figure 3-19).

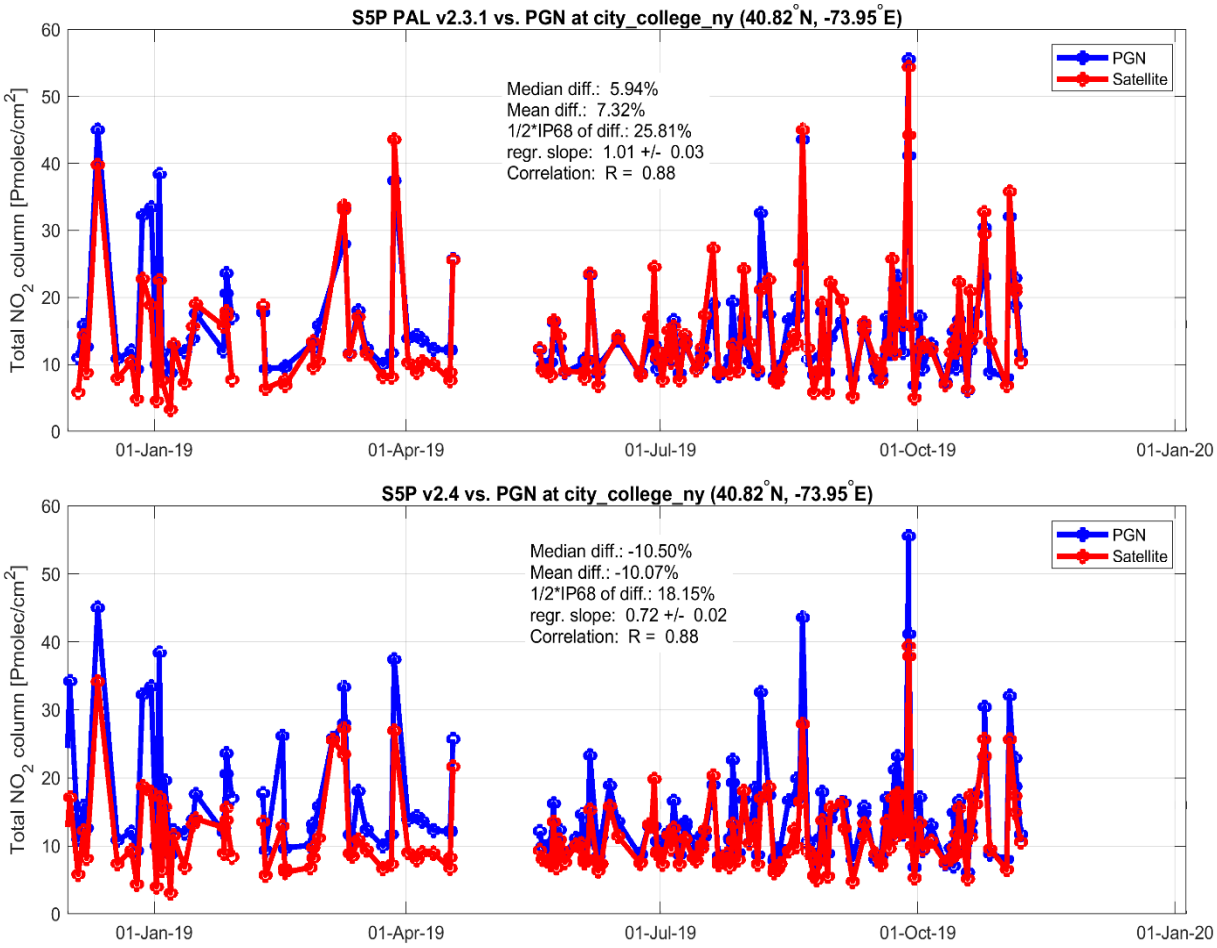


Figure 3-18: Temporal subset of the S5P vs. PGN comparisons at City College, New York, for the PAL v2.3.1 data in the top panel and for the v2.4 data in the bottom panel.

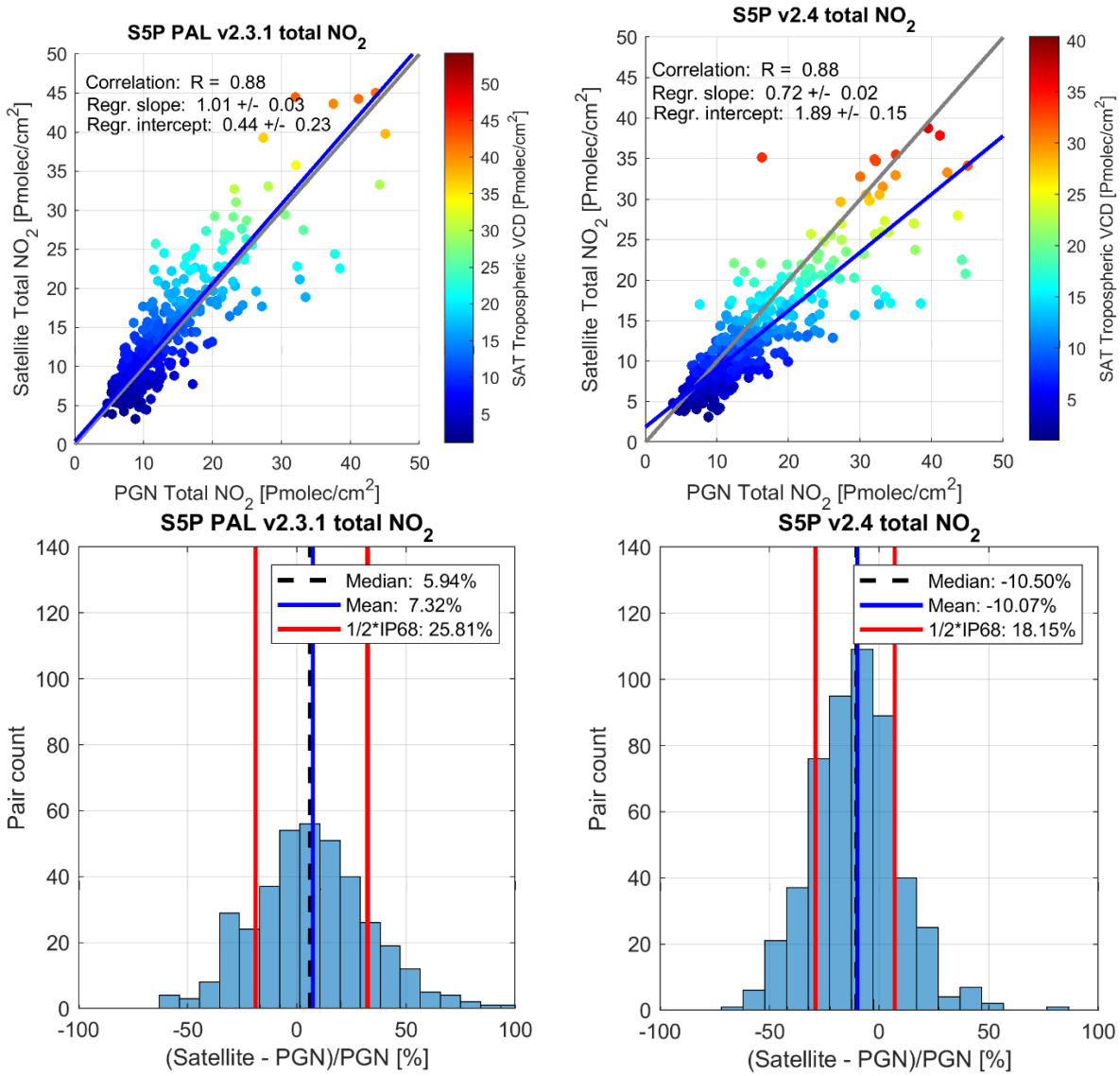


Figure 3-19: Scatter plots and histograms corresponding to the analysis at City College, New York, for PAL v2.3.1 on the left-hand side and v2.4 on the right-hand side. Most notable are the reduced dispersion but increased multiplicative underestimation in v2.4.

It is not clear from the current analysis how this relates to the processor changes between v2.4 and v2.3.1. Surface albedo ranges are only slightly larger in the v2.4 product.

3.6 Algorithm selection

4 Separation of stratosphere and troposphere for NO_2

4.1 Data and algorithms used

4.1.1 Data

4.1.1.1 GEMS

We investigate different stratospheric estimation schemes based on GEMS data for 4 months in 2021 (January, April, July, October). Two GEMS versions are used:

- the operational GEMS product v3.0 (Lee et al., 2024), and
- the IUP Bremen product v1.0 (Lange et al., 2024) discussed in section 5, with two different variants for the stratospheric correction.

4.1.1.2 TROPOMI

TROPOMI level 2 data is used for comparison of stratospheric patterns and tropospheric residues. Here we use the reprocessed data (RPRO 2.4).

In addition, a gridded temporal mean is used for defining regions free from tropospheric pollution. Here we use the full temporal mean of the PAL product, covering May 2018 to November 2021.

4.1.1.3 EMAC

We use the numerical global atmospheric chemistry model EMAC (ECHAM/MESSy Atmospheric Chemistry) to develop an empirical stratospheric correction scheme (see section 4.1.2.3). EMAC data are used here to examine typical dependencies of stratospheric VCDs on longitude, latitude, and, in particular, time of day. This dataset was provided by Matthias Kohl and Andrea Pozzer from MPIC Mainz.

4.1.2 Algorithms

4.1.2.1 Operational GEMS product

The stratospheric correction of the operational GEMS product is described in Lee et al. (2024). It is based on the algorithm described in Bucsela et al. (2013), which estimates the stratospheric column from all satellite pixels where the tropospheric column modeled by GEOS-CHEM is below a threshold. However, as shown in Lee et al. (Fig. 5 therein), with the initial threshold value, no valid data is left over large parts of South Korea, China, and Japan.

4.1.2.2 MPIC STREAM

The STRatospheric Estimation Algorithm from Mainz (STREAM) has been developed at MPIC Mainz as part of the TROPOMI verification activities (Beirle et al., 2016). STREAM is a modified reference sector method, i.e. the stratospheric column is derived from measurements over clean regions. Additional information on the stratospheric column is gained from cloudy pixels, where the tropospheric column is shielded. This is realized by defining weights for individual TROPOMI pixels determining how far the measured total column should be considered as a proxy for the stratospheric column, and subsequent weighted convolution.

A further feature of STREAM is an iterative correction scheme: in case of (unphysical) negative tropospheric residues, the local stratospheric column must have been overestimated, and the respective pixel gets a higher weight for the next iteration.

STREAM has been successfully applied to TROPOMI measurements (Beirle et al., 2016). We have tried to apply STREAM for GEMS. However, this turned out to be challenging:

- clean reference regions are very sparse within GEMS spatial coverage. In particular for the highly polluted regions in South Korea and Eastern China, reference measurements East- and Northwards are missing.
- over large parts of China, also clouded pixels are often polluted, and have to be masked by the pollution mask. Consequently, the information from clouded observations is missing for GEMS.
- due to the large noise of the GEMS DOAS retrieval, there is a significant number of outliers in the GEMS level 2 data. If the tropospheric residue weight would be applied to such noisy data, outliers to lower values would receive a larger weight, resulting in an overall low-biased stratospheric estimate by the STREAM iterative approach.

Thus, we conclude that STREAM, as presented in Beirle et al. (2016), cannot be directly applied to GEMS data.

4.1.2.3 MPIC empirical correction (EC)

A dedicated empirical stratospheric correction for GEMS has been developed within this project. The aim is to define a rather simple and robust measurement-based stratospheric estimation for GEMS that might not catch every detail of stratospheric NO_2 patterns, but on average reflects the dependencies on latitude, longitude and time of day appropriately.

According to EMAC model results, longitudinal variations of the stratospheric column in the region covered by GEMS are generally small: The longitudinal standard deviation of monthly mean stratospheric VCDs is up to 10^{14} molec/cm^2. This is far lower than the longitudinal variability of tropospheric VCDs. Thus, within MPIC EC, longitudinal variations of the stratospheric VCD are not considered.

The time-of-day dependency of the stratospheric VCD is a key property of measurements from geostationary satellites, and it needs to be corrected appropriately before potential time-of-day variations of tropospheric columns can be analyzed quantitatively.

Stratospheric NO_2 generally increases during the day due to photodissociation of N_2O_5. Several studies report that this can be described by a linear increase of about 10^{14} molec/cm^2/h (Flaud et al., 1988; Sussmann et al., 2005; Gil et al., 2008; Li et al., 2021). We have used EMAC data to investigate this dependency for different months as a function of latitude, and derive the slope of the linear increase for each month and latitude by a linear fit to the EMAC stratospheric column. Figure 4-1 displays the resulting slopes derived from EMAC, where literature values have been added as well.

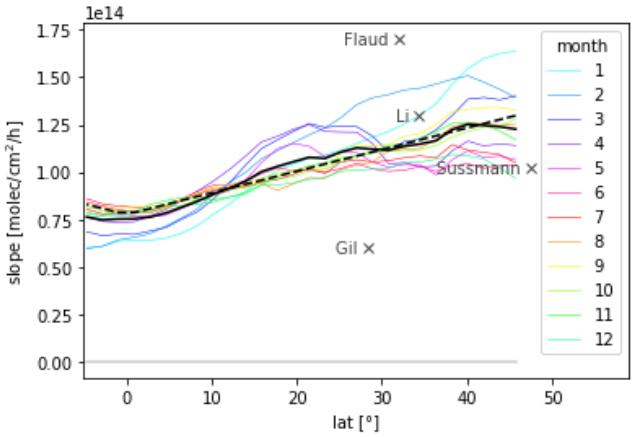


Figure 4-1: Slope of the linear increase of stratospheric NO2 for different months as a function of latitude, derived from a linear fit to EMAC data. Literature values are added as crosses. The dashed line displays the parameterization of Eq. 1.

We conclude that the slope increases with latitude, and that seasonality is a second-order effect here. For the simplified EC scheme, we thus parameterize the slope as a function of latitude only:

$$s(lat) = (7.761*10^{13} + 1.142*10^{12}*|lat[°]|)\ molec/cm^2/h \qquad \text{(Eq. 1)}$$

As for STREAM, EC is based on the total SCD divided by the stratospheric AMF:

$$V^* = SCD/AMF_{strat} \qquad \text{(Eq. 2)}$$

In the case of no tropospheric pollution, V* represents the stratospheric column.

With the parameterized slope (Eq. 1), V* can be converted into a “noon-time equivalent V*” (NTEV) for each pixel. In EC, the daily noon-time stratospheric column is then simply estimated as the minimum NTEV along the longitude for each latitude bin across all frames of one day. The assumption is that for each latitude, there is some longitudinal range with negligible tropospheric pollution.

For the stratospheric correction of individual pixels, the daily noon-time stratospheric column is then again adjusted to local time according to Eq. 1.

4.1.2.4 IUP Bremen "STREAM"

A variant of the STREAM algorithm called STREAM-UB is also evaluated. It differs from the original STREAM algorithm developed by Beirle et al., 2016 in three aspects:

1. The pollution mask is not static but derived from the tropospheric NO_2 field modelled by the TM5 model run for the TROPOMI processor (Williams et al., 2017) for the respective day
2. Information from cloudy pixels is not used
3. Over the clean regions used for the estimation of the stratospheric column, the tropospheric slant column derived from the TM5 model is subtracted from the measured slant columns. This accounts for the tropospheric background and replaces information from cloudy pixels.

4.1.2.5 IIUP Bremen "TM5"

Finally, the stratospheric NO_2 column from the TM5 model run for the TROPOMI data product is used directly. These data are obtained from a TM5 run with a simple stratospheric NOy chemistry

and assimilation of NO_2 columns from TROPOMI. At the time of TROPOMI overpass, these values are identical to the stratospheric column used in the operational TROPOMI product.

4.2 Comparison

Here, we present a systematic evaluation of the different stratospheric estimation schemes. In the following, two quantities are analyzed:

- the stratospheric VCD V_{strat}, and
- the tropospheric residues TR = V* – V_{strat}

For all algorithms, the L2 data from each frame is gridded on a regular 1°x1° grid by taking the median of all L2 values within the grid pixel. By this procedure, outliers from the DOAS analysis are mostly removed.

4.2.1 Spatial patterns

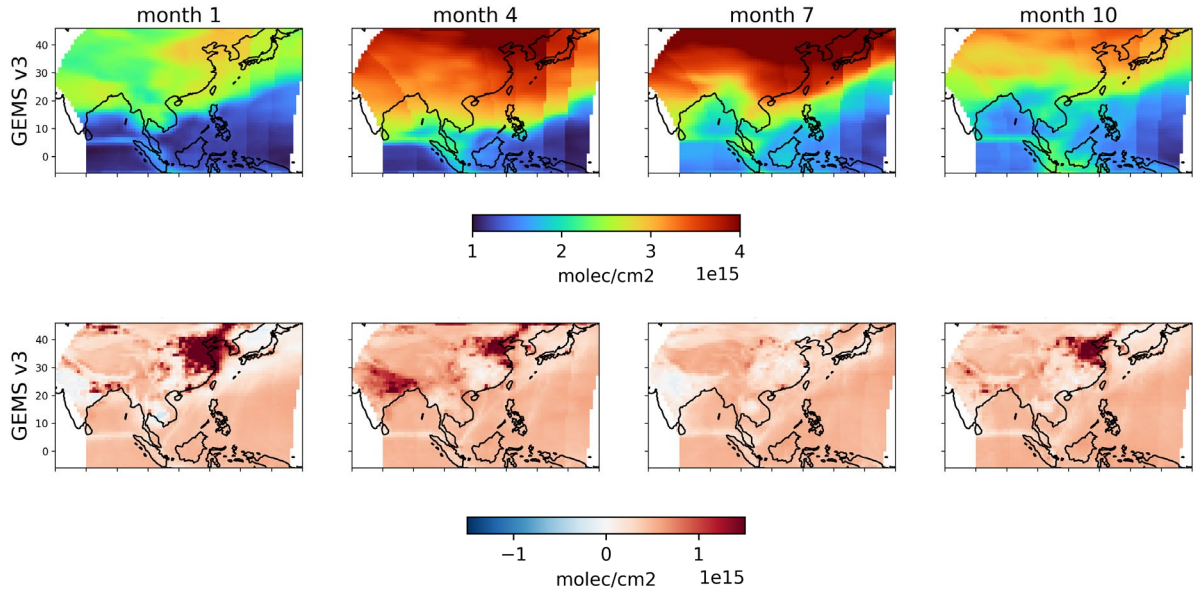


Figure 4-2: Monthly mean V_{strat} (top) and TR (bottom) for the GEMS v3 operational product.

Figure 4-2 displays maps of V_{strat} and TR for the investigated months for the operational GEMS product v3.0. Generally, the operational stratospheric VCD is quite high. In particular, regions with high tropospheric background in e.g. China or India show enhanced V_{strat}. Most strikingly, the highly frequented ship track South of the Bay of Bengal is visible in the stratospheric VCD. Consequently, TRs are quite low and can even be negative over India, China, and the ship tracks. Thus, it has to be concluded that the stratospheric correction applied in GEMS v3.0 does not work as intended, as the GEMS pixels that have been used for the stratospheric estimation still contain significant tropospheric pollution, which then wrongly ends up in the stratospheric column. In the comparisons below, the operational GEMS product is therefore not included.

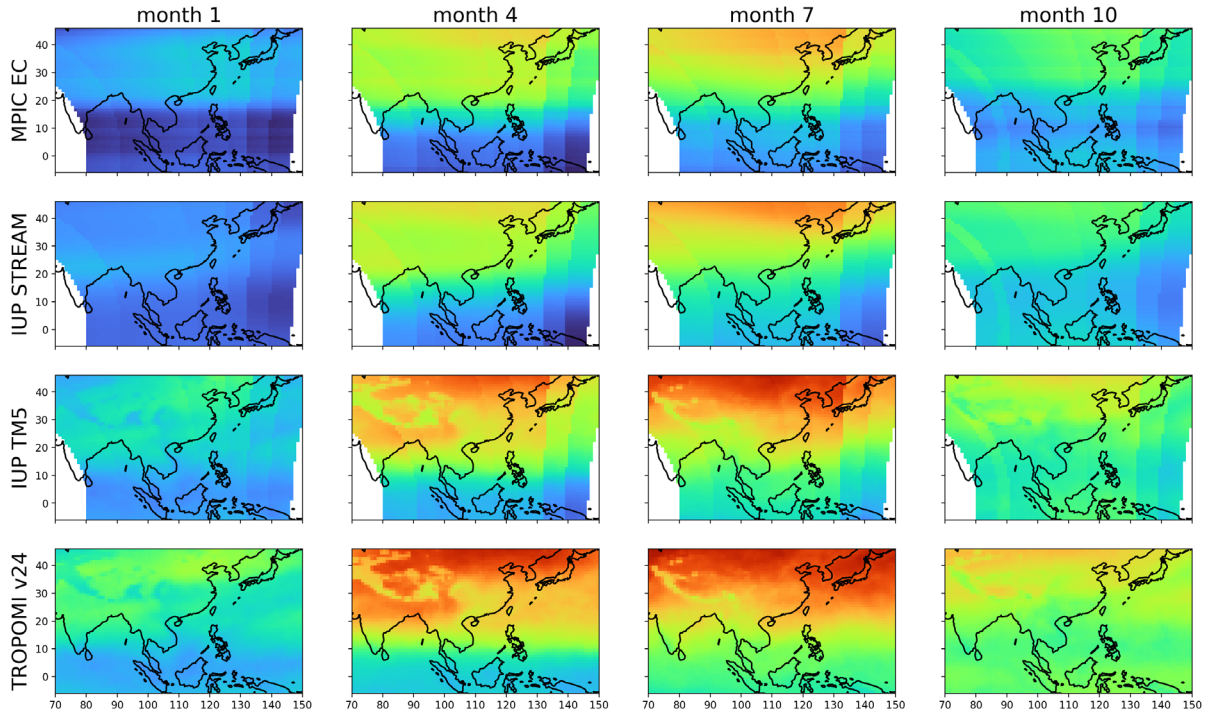


Figure 4-3: Monthly mean V_{strat} for the investigated algorithms applied on GEMS data, and the TROPOMI operational product. Colorbar as in Fig. 4.1.

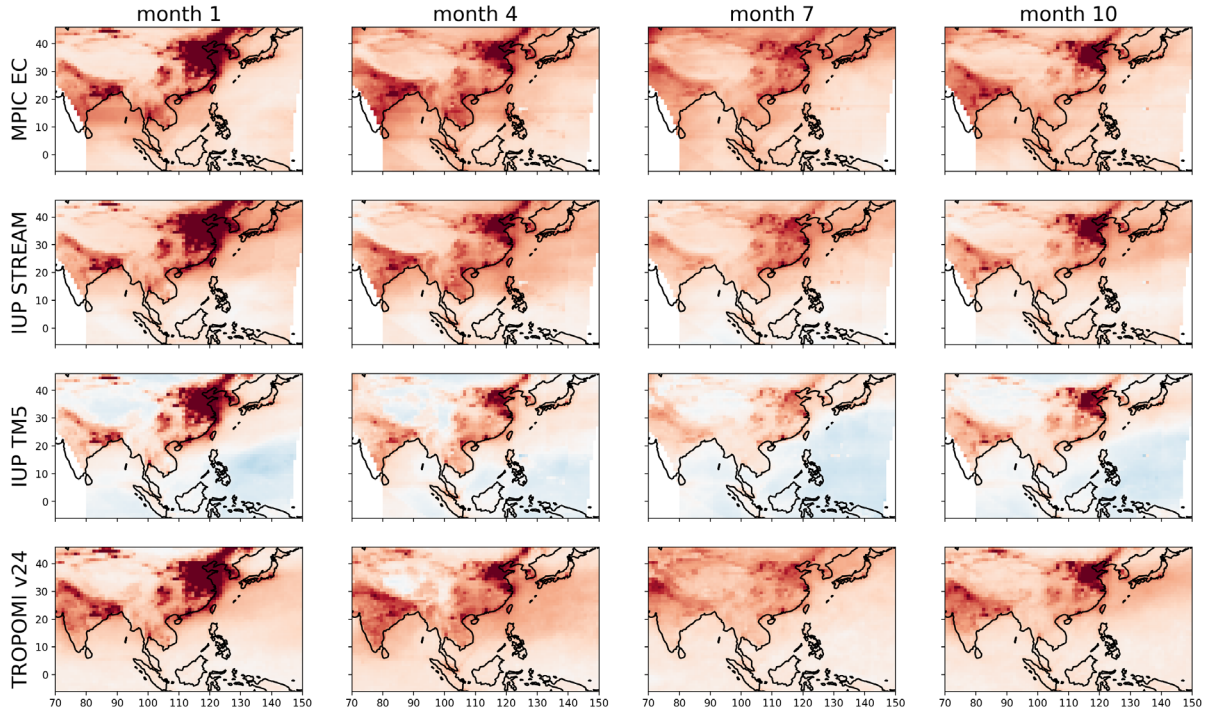


Figure 4-4: Monthly mean TR for the investigated algorithms applied on GEMS data, and the TROPOMI operational product. Colorbar as in Fig. 4.1.

Figure 4-3 displays monthly means of the stratospheric VCD for MPIC EC, IUP STREAM and IUP TM5. For comparison, the TROPOMI v2.4 mean is also shown. Overall, all methods yield

comparable spatial patterns. In particular, MPIC EC and IUP STREAM are very similar. IUP TM5 has generally higher values. Note that the TROPOMI mean is higher than the IUP TM5 mean (using the TM5 column assimilated with TROPOMI). This is due to averaging measurements across all available times of day for IUP TM5, whereas in the TROPOMI product, only measurements at TROPOMI overpass around 2 p.m. local time are averaged.

In Figure 4-4, the corresponding tropospheric residues are shown. Again, the spatial patterns are quite similar, and the regions with high tropospheric pollution are clearly visible for all algorithms. Due to the higher stratospheric VCD in IUP TM5, the corresponding TRs are lower than those of the other algorithms and are even negative over large parts of the GEMS area.

4.2.2 Dependency on latitude

Figure 4-5 displays the monthly mean stratospheric VCD from the different algorithms as a function of latitude. In addition, the stratospheric column from TROPOMI and the EMAC model is displayed. All algorithms yield similar dependencies that also match the EMAC model, with offsets between the algorithms as discussed above.

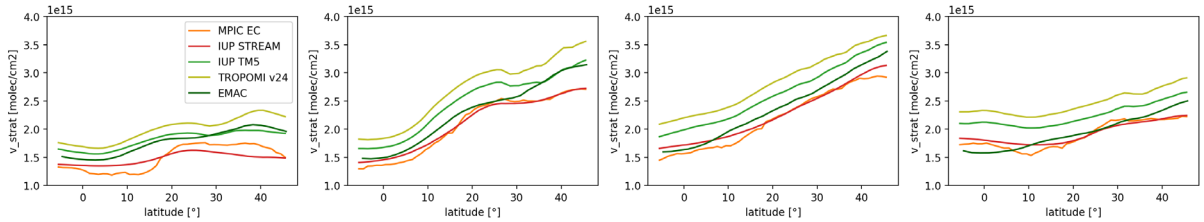


Figure 4-5: Monthly mean stratospheric VCD as a function of latitude.

4.2.3 Dependency on time of day

The dependency of V_{strat} on time of day is shown in Figure 4-6 for 34.5° N, 126.5° E. All products clearly show the increase of stratospheric NO_2 with time of day. For MPIC EC, this increase is exactly linear by construction, as the method is based on the parameterization in Eq. 1. IUP STREAM shows discontinuities in the morning hours. This is caused by the change of field of view of the GEMS instrument during the day and the fact that IUP STREAM estimates the stratospheric VCD for each frame independently. Note that with TROPOMI, only small variations of time of day are covered, and the measurements with early/late time of day correspond to the TROPOMI swath edges with different satellite viewing angles and relative solar azimuth angles. As a result, any systematic effect of viewing geometry on BRDF, cloud product etc. could affect this dependency.

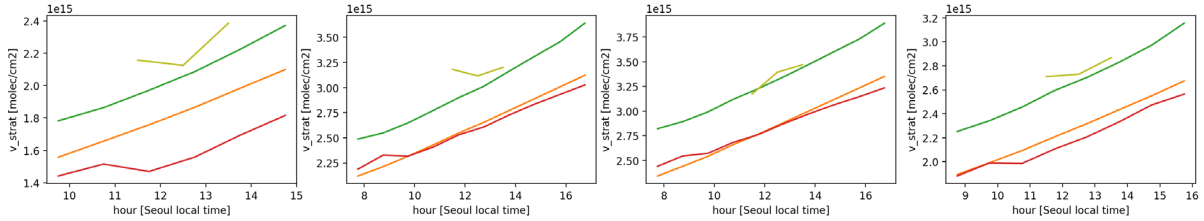


Figure 4-6: Monthly mean stratospheric VCD at 34.5° N, 126.5° E as a function of time of day. Colors as in Fig. 4.5.

4.2.4 Distribution of tropospheric residuals over clean regions

The accuracy and precision of the stratospheric correction can be assessed by analyzing TRs over regions without significant tropospheric sources; here, TRs should have low mean values and low standard deviations.

The exact value of the expected TR cannot be derived from the satellite measurements alone and requires additional information from models or independent measurements. However, significantly enhanced or negative TRs clearly indicate stratospheric estimates that are too low/too high.

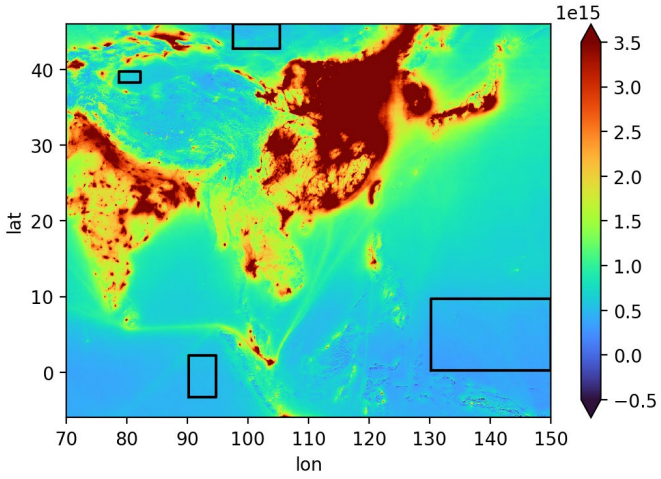


Figure 4-7; Temporal mean tropospheric VCD (May 2018-November 2021) from the TROPOMI PAL product. Black rectangles indicate the "clean" regions (Table 4.1).

Table 4-1: "Clean" reference regions.

Name	lat 1	lat 2	lon 1	lon2
Takla Makan	38.25	39.75	78.75	82.25
Gobi	42.75	46.0	97.5	105.25
Indian Ocean	-3.25	2.25	90.25	94.75
Pacific	0.25	9.75	130.25	150.0

Based on the long-term averaged TROPOMI tropospheric VCD (Figure 4-7), we define 4 "clean" regions (Table 4-1), two over deserts in Asia and two over the ocean. Figure 4-8 displays frequency distributions of TRs for these regions.

The distribution width of all algorithms is quite similar. Mean tropospheric residues from MPIC EC, IUP STREAM, and TROPOMI operational product are also similar, while TRs from IUP TM5 are significantly lower and often negative.

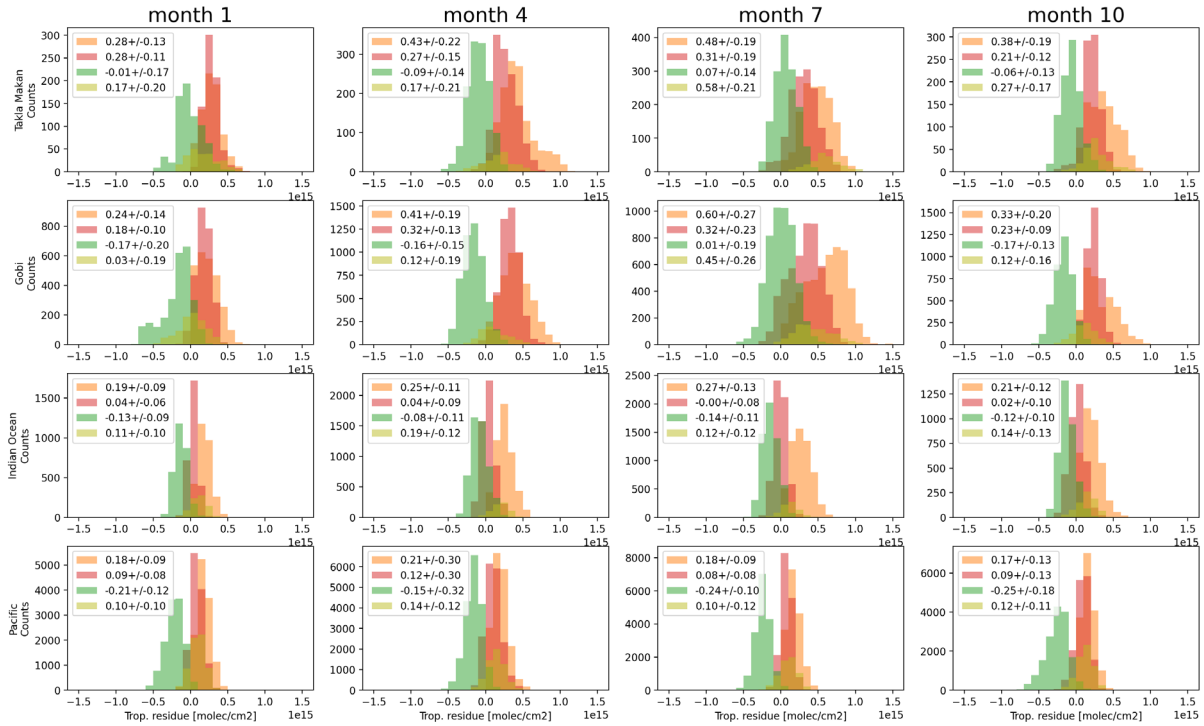


Figure 4-8: Frequency distribution of TRs for the investigated reference regions. Colors as in Fig. 4.5.

4.3 Algorithm selection

We have demonstrated that stratospheric correction for GEMS can be performed by empirical approaches based on GEMS measurements themselves, like MPIC EC or IUP STREAM. However, in contrast to previous empirical corrections, the tested algorithms are not completely independent from models any more:

- MPIC EC corrects for the diurnal increase of stratospheric NO_2 based on a simple linear function with slopes fitted to EMAC data.
- IUP STREAM uses TM5 data for defining the pollution mask and for correcting for tropospheric contribution

In addition, the current algorithms have some issues that need to be fixed:

- MPIC EC needs to apply some more advanced data processing, like smoothing along latitude.
- IUP STREAM estimates stratospheric VCD for each frame individually. This results in discontinuities in the diurnal cycle when the GEMS FOV is switched.

Correcting the stratospheric VCD based on model simulations, here TM5 (assimilated to TROPOMI), works generally well, but with the initial version, resulting TRs over clean regions are too low, and often even negative. This should be improved by subtracting an offset (fixed in terms of SCD?) from the TM5 stratospheric VCD before applying it to GEMS data.

For this project, we recommend applying a modified TM5 correction scheme, which is well-defined, transparent, and easily adoptable for other sensors such as TEMPO or S4. There is, however, one risk with this approach: the TROPOMI time series might stop, and the assimilated TM5 stratospheric VCD will no longer be available.

5 GEMS NO_2

5.1 Data and algorithms used

The GEMS data used in this report are from two sources: The operational GEMS products in different versions, provided by NIER, and the IUP Bremen scientific GEMS data product v1.0 (Lange et al., 2024), which can also be created with flexible input options.

The IUP Bremen GEMS NO_2 product v1.0 applies a standard DOAS retrieval including terms for the correction of scene inhomogeneity effects, performs the stratospheric correction using STREAM-UB, a variant of the STREAM algorithm by Beirle et al., 2016 and uses air mass factors computed with a SCIATRAN-based LUT, the TROPOMI LER climatology v1.1, and the TM5-MP model run for TROPOMI as a priori. As the current operational GEMS v3.0 cloud product still has some issues, cloud fractions are recalculated using the CLUMSY algorithm (Zien et al., 2014) and cloud pressures from the GEMS product. Several of these parameters are varied in the following sections.

5.2 Surface reflectance

Enhancing the precision of L2 algorithms relies heavily on the accurate estimation of the surface reflectance. The surface reflectance depends on geometry and the bidirectional reflectance distribution function (BRDF). For LEO satellites, this can be accounted for by using the Differential Lambertian Equivalent Reflectivity (DLER), determined from measurements of the same satellite (e.g. TROPOMI, Tilstra et al. 2024). For GEO satellites, this is less straightforward, as solar angles change over the day. The solution is to use a BRDF model and calculate the corresponding LER for each measurement. The BRDF model can be from GEO measurements themselves, or in principle also from LEO observations. As the observational geometries of GEMS and TROPOMI are not the same, the directionally dependent LER (DLER) climatology, based on TROPOMI observations, cannot be used for GEMS.

The operational GEMS NO_2 product accounts for BRDF effects by using the GEMS Background Surface Reflectance (BSR) product, a semi-empirical bidirectional reflectance distribution function (BRDF) model (Sim et al. 2024). Since the GEMS BSR product showed large differences to surface reflectance products from other sensors, the first version of the GEMS IUP-UB product used the TROPOMI LER product (Lange et al. 2024). To investigate the effect of the surface reflectance on the GEMS NO_2 product, different surface reflectance products (GEMS L2 v3 BSR, TROPOMI LER, and MODIS BRDF-based LER) have been tested within the GEMS IUP-UB NO_2 retrieval.

Figure 5-1 shows scatterplots of GEMS vs. co-located ground-based (more details in Section 5.5) NO_2 tropospheric VCDs of (a) the operational GEMS L2 v3.0 NO_2 tropospheric VCD product using the GEMS L2 v3.0 BSR product in the AMF calculation, (b) the GEMS IUP-UB NO_2 tropospheric VCD product using the TROPOMI LER v1 reflectivity, and (c) the GEMS IUP-UB NO_2 tropospheric VCD product using the GEMS L2 v3.0 BSR. The comparison shows that the GEMS L2 v3.0 BSR product introduces significantly more scatter to the NO_2 product and an overestimation of the NO_2 tropospheric VCDs compared to the ground-based observations. This overestimation is not

visible in the GEMS L2 v3.0 product, indicating that the effect of the surface reflectivity might be compensated by high biased stratospheric columns (see section 5.4).

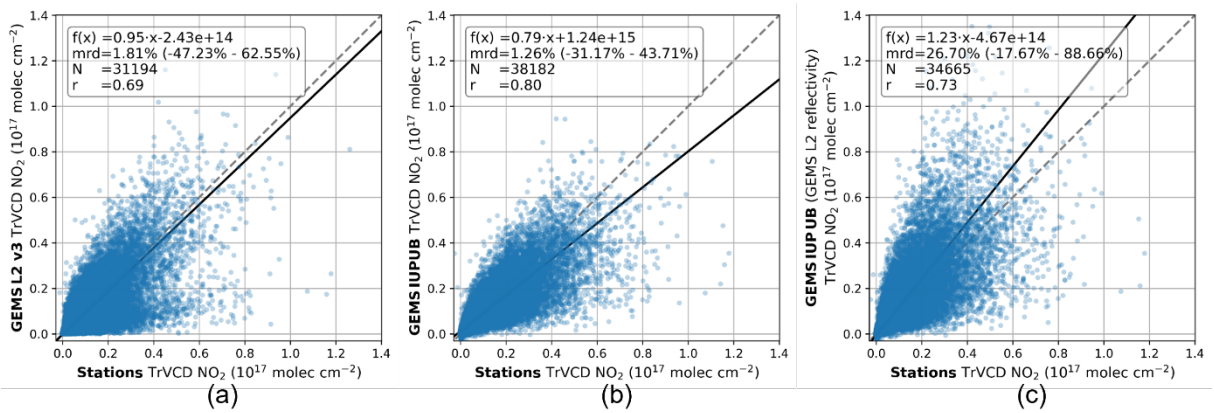


Figure 5-1: Scatterplots of satellite vs. co-located ground-based NO_2 tropospheric VCDs for (a) the GEMS L2 v3.0 product using the GEMS L2 surface reflectance observations, (b) the original GEMS IUP-UB product using the TROPOMI LER v1, and (c) the GEMS IUP-UB product using the GEMS L2 v3.0 reflectance data.

Figure 5-2 shows the average of the GEMS L2 v3.0 BSR product, the TROPOMI LER v1 used in the GEMS IUP-UB NO_2 product, and the difference between both products for October 2022 for scan 00:45 UTC, 03:45 UTC, and 06:45 UTC. The largest deviations between the GEMS L2 v3.0 BSR and the TROPOMI LER are visible for Indonesia, Cambodia, and the south of Vietnam and Thailand, where GEMS shows brighter scenes over land. For most of the remaining area, the GEMS BSR used in v3.0 is lower than the TROPOMI LER. The GEMS BSR used in the GEMS L2 NO_2 product v4.0.1 is identical to v3.0. Qualitative agreement between the TROPOMI LER and GEMS v3.0 BSR improved compared to v2.0 (not shown here).

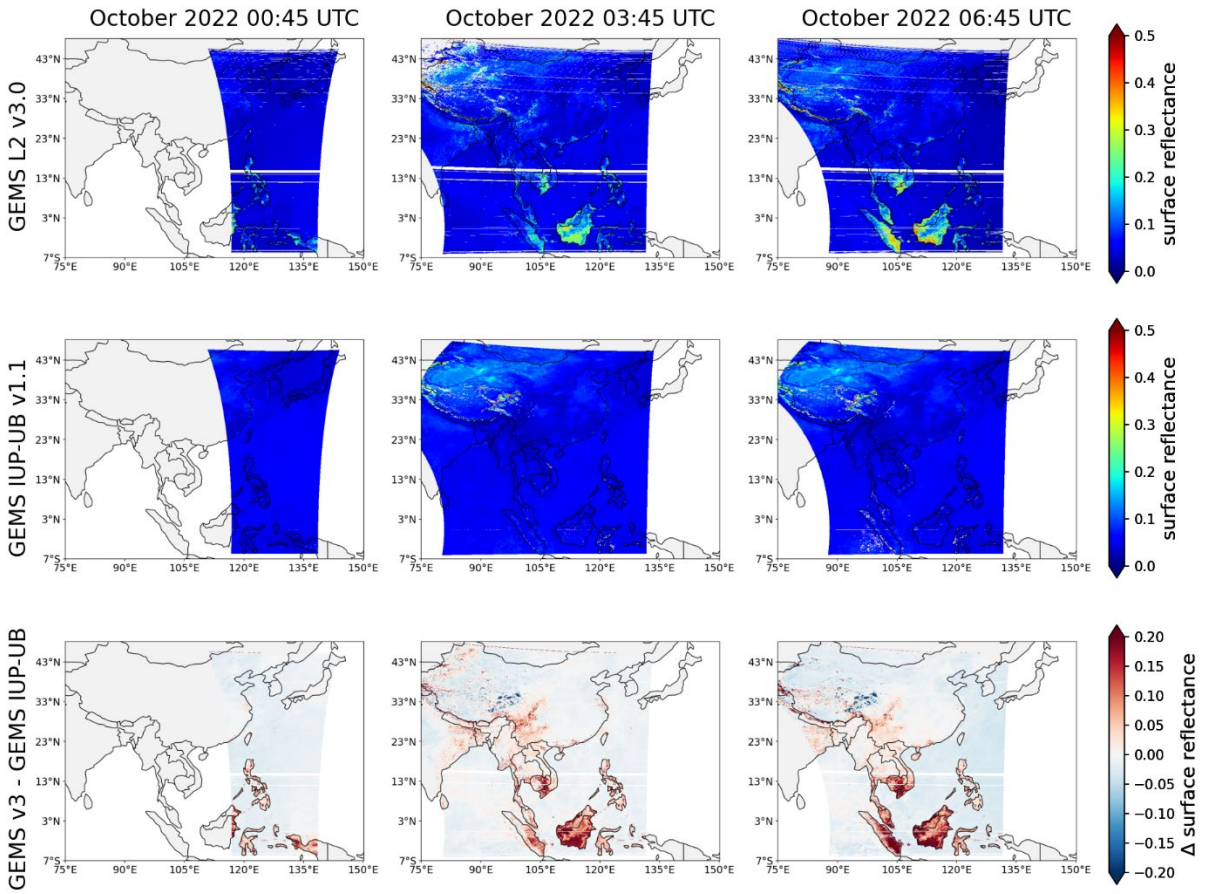


Figure 5-2: Monthly average of the surface reflectance products for October 2022 at 00:45 UTC, 03:45 UTC, and 06:45 UTC for GEMS L2 v3.0 (top row, GEMS L2 BSR), GEMS IUP-UB (middle row, TROPOMI LER), and the difference of the GEMS v3.0 – GEMS IUP-UB surface reflectance products (bottom row).

Since these analyses showed that the GEMS BRDF-based surface reflectance product is not yet reliable enough, a different approach was tested using the MODIS BRDF product. For the MODIS BRDF-based LER approach, the GEMS geometry and MODIS BRDF coefficients f_{iso}, f_{vol}, f_{geo} at 440 nm are needed. The approach followed the ideas of Vasilkov et al., 2017 to use the modelled top of atmosphere reflectance to find the appropriate surface LER for a given measurement. A fast LUT-based approach for this BRDF treatment was developed for the ITMS TROPOMI NO_2 product and applied here to GEMS data.

Comparisons of the MODIS BRDF-based LER and the TROPOMI LER should provide decision support on which of the surface reflectance products should be used for the GEMS NO_2 product. Using the TROPOMI LER in the GEMS NO2 product would increase consistency with the LEO NO2 products developed in the first phases of the project. However, the MODIS BRDF-based product is expected to perform best regarding the GEO geometry variations.

Figure 5-3 shows the distribution of the TROPOMI LER v2-2, the MODIS BRDF-based LER, and their difference on 15 January 2023 for the 01:45, 03:45, and 05:45 UTC GEMS scans. The largest deviations are found in the northern part of the scan, especially the north-west, where the most extreme observation geometries coincide with snow/ice conditions, with MODIS providing mostly larger surface reflectance values.

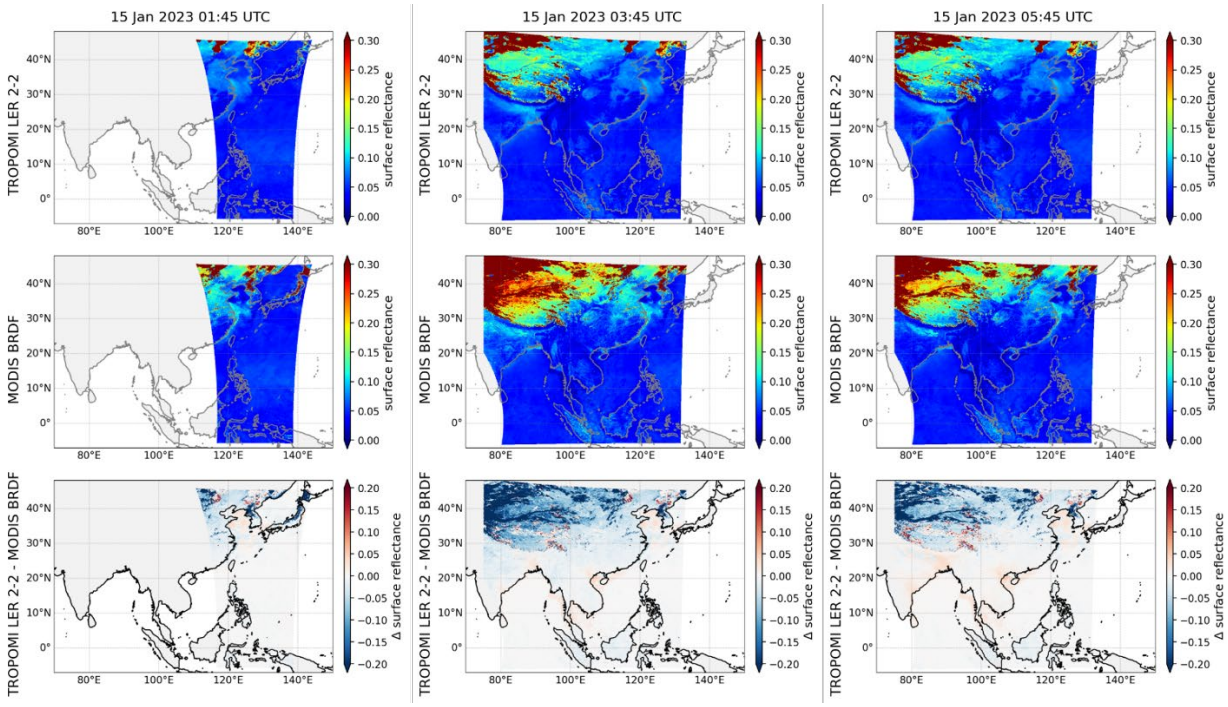


Figure 5-3: Surface reflectance maps of the TROPOMI LER v2-2 (top row), the MODIS BRDF-based LER (middle row), and their difference (bottom row) for 15 January 2023 for the 01:45, 03:45, and 05:45 UTC GEMS observation time.

The MODIS BRDF-based LER is a 16-day sliding average capturing actual snow conditions. While the TROPOMI LER v2-2 contains separate snow/ice and snow-free monthly climatologies at a resolution of 0.125° x 0.125° derived from 7 years of TROPOMI observations, and the respective climatology is selected using a snow/ice flag. For the rest of the GEMS domain, the MODIS BRDF-based LER agrees closely with the TROPOMI LER. There are only a few areas where the MODIS-based surface reflectance results in higher values than the TROPOMI LER. Because the TROPOMI LER climatology is derived from the lower end of the TROPOMI scene brightness distribution, it represents a relatively low-reflectance surface. Deviations are similar between scans. For the 03:45 UTC scan, the mean value for the TROPOMI LER v2-2 product is 0.08, while the MODIS BRDF-based LER mean value is 0.13, resulting in a mean difference between the two products (TROPOMI - MODIS) of -0.04 ± 0.12. Analyses of seasonal differences for April, July, and October showed that there is overall better agreement in April and July while the October comparisons look again more similar to January (not shown here).

Figure 5-4 shows time series for individual pixels in different areas of the GEMS domain (Seoul, Singapore, and central India) for one individual day in each season (15 January, 15 April, 15 July, and 15 October 2023) over the course of the day. As shown, the MODIS BRDF-based LER is generally higher than the TROPOMI LER, especially for the Seoul pixel in January and October. The MODIS product shows higher diurnal variability, while the TROPOMI LER diurnal cycle is, as expected, very flat. As there is no angular variation in the TROPOMI LER, any changes are the result of different spatial sampling. For the selected pixel in central India, the TROPOMI LER is higher than the MODIS BRDF-based LER in April for all five observation times of the day.

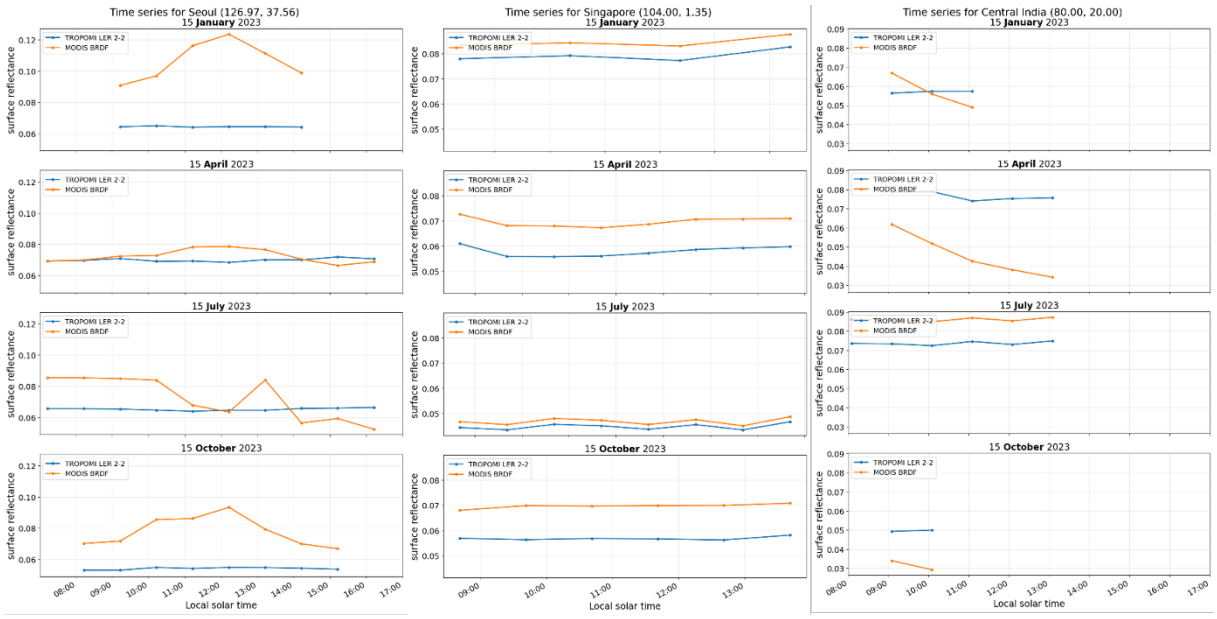


Figure 5-4: Time series of the surface reflectance of the TROPOMI LER v2-2 (blue) and the MODIS BRDF-based LER (orange) for a selected pixel in Seoul (left), Singapore (middle), and central India (right) for one individual day in each season (15 January, 15 April, 15 July, and 15 October 2023).

5.3 Clouds

Cloud parameters are important both for the NO_2 retrieval itself and for filtering of cloud-contaminated scenes for scientific applications and validation. The operational GEMS cloud product is an O_2-O_2 cloud product retrieved in the 460-485 nm window (Kim et al. 2024).

Figure 5-5 shows the cloud fraction on 15 April 2021 of the O_2-O_2 GEMS L2 v3.0 for the 03:45 UTC scan and the cloud radiance fraction in the NO_2 window of the TROPOMI L2 v2.4 NO_2 product and their difference. Differences are quite large, with up to ±0.5. For large areas, the TROPOMI cloud fraction is significantly lower than that of GEMS. The histogram distribution plots in Figure 5-5 (right) show that the GEMS cloud fraction has a broader distribution with only a few clear-sky scenes (cloud fraction of 0), while the TROPOMI distribution shows many more clear-sky scenes and fewer fully cloudy pixels. Comparing the GEMS O_2-O_2 cloud fraction product with the TROPOMI O_2-O_2 product, the agreement is improved, but mainly for fully cloudy scenes, while discrepancies are still large for clear-sky scenes (not shown here). The GEMS L2 NO_2 v3.0 and v4.0.1 show identical cloud parameters, which are assumed to be based on the v3.0 cloud product. GEMS L2 v4.0 differs from v4.0.1 and v3.0 due to the use of an erroneous surface reflectance in v3.0 (not shown here).

Figure 5-6 shows cloud pressure maps on 15 July 2024 for the GEMS L2 v3.0 for the 03:45 UTC observation and the TROPOMI v2.6 FRESCO product (left) and the TROPOMI v2.6 O_2-O_2 product (right). Differences are large, showing positive and negative biases and are only slightly reduced when comparing both O_2-O_2 cloud pressure products.

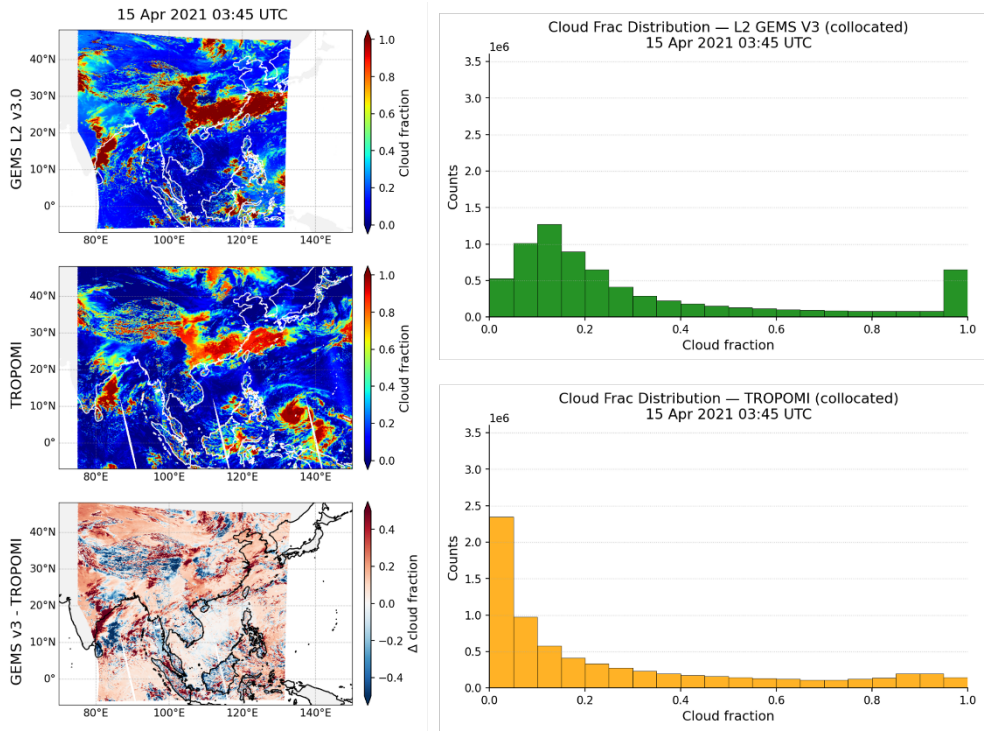


Figure 5-5: (left) Cloud fraction maps on 15 April 2021 for the GEMS L2 v3.0 for the 03:45 UTC observation and the TROPOMI v2.4 product and their differences. (right) Corresponding distribution histograms of the cloud fractions.

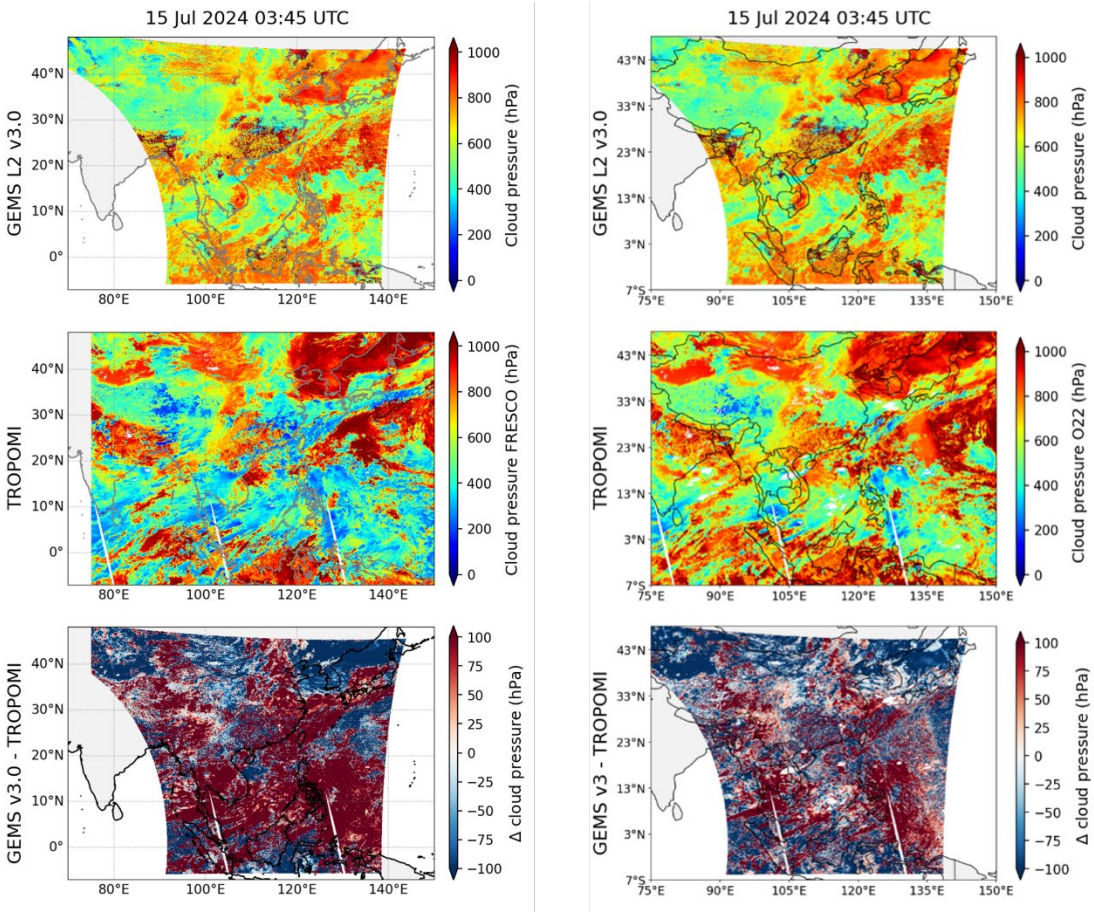


Figure 5-6: Cloud pressure maps on 15 July 2024 of the GEMS L2 v3.0 for the 03:45 UTC observation and the TROPOMI v2.6 FRESCO product (left) and the O_2-O_2 product (right) and their differences.

Due to observed inconsistencies in cloud statistics and discrepancies with other cloud products, a simple cloud fraction algorithm was implemented for the GEMS IUP-UB NO_2 product, using TROPOMI LER and GEMS reflectivity within the NO_2-fitting window to derive a cloud fraction. As GEMS irradiances suffer from calibration issues, they were scaled to TROPOMI irradiance measurements before computing the reflectance. Since this simple algorithm cannot retrieve cloud heights, the GEMS IUP-UB product has to use the operational cloud pressure.

Figure 5-7 shows the cloud fraction distributions for the operational GEMS L2 product, the GEMS IUP-UB product and the TROPOMI product, illustrating that the cloud fraction algorithm of the GEMS IUP-UB retrieval results in cloud fractions significantly closer to the TROPOMI distribution, especially for lower cloud fractions.

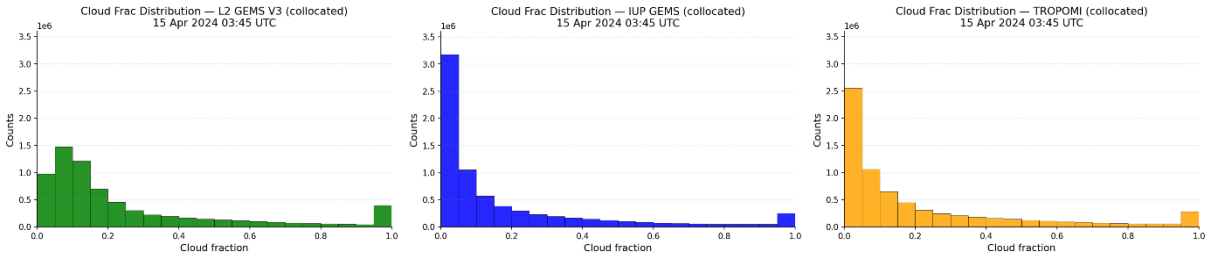


Figure 5-7: Cloud fraction distributions for 15 April 2024 for the 3:45 UTC scan for the operational GEMS L2 v3.0 O_2-O_2 cloud fraction (green), the GEMS IUP-UB cloud radiance fraction in the NO_2 window (blue), and the collocated TROPOMI cloud radiance fraction in the NO_2 window for that day (yellow).

The cloud fraction differences between the operational GEMS and the GEMS IUP-UB cloud fraction show similar behaviour over the course of the day and across seasons.

In a further analysis, the sensitivity of the retrieved cloud fraction to the selected surface reflectance product was assessed. Figure 5-8 shows the cloud fraction for 15 April 2023 of the three scans 00:45, 03:45, and 06:45 UTC, derived for the GEMS IUP-UB cloud algorithm using either the TROPOMI LER v2-2 or the MODIS BRDF-based LER (see section 5.2). Overall, the MODIS BRDF-based cloud fractions are smaller than the TROPOMI LER-based cloud fractions, with up to 0.2 to 0.4 differences in the extreme geometries. The differences vary slightly from scan to scan, with the largest differences in the early scan and for the most extreme geometries. Overall, the cloud fractions from the two surface reflectance approaches are comparable, with differences mostly below 0.1.

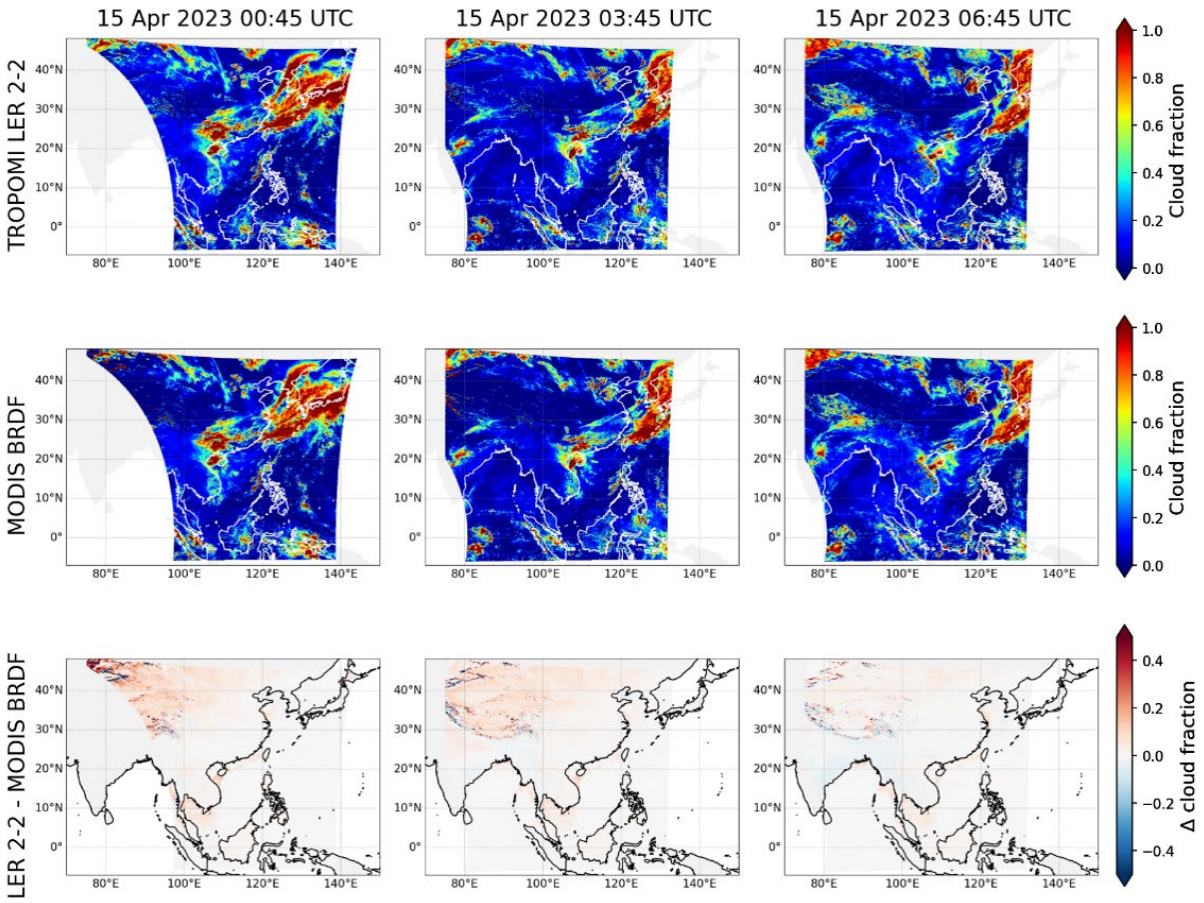


Figure 5-8: Cloud fraction for 15 April 2023 of the scans 00:45 UTC (left column), 03:45 UTC (middle), and 06:45 UTC (right) for the GEMS IUP-UB cloud algorithm based on the TROPOMI LER v2-2 (top row) and the MODIS BRDF-based LER (middle row), and their differences (bottom row).

5.4 Separation of stratosphere and troposphere

The contribution of the stratosphere, with column densities on the order of 10^{15} molec. cm^{-2} is not very large in polluted regions but is of greater importance at less polluted sites. The diurnal variation in the stratospheric NO_2 VCD products is shown as an example for Seoul in Figure 5-9.

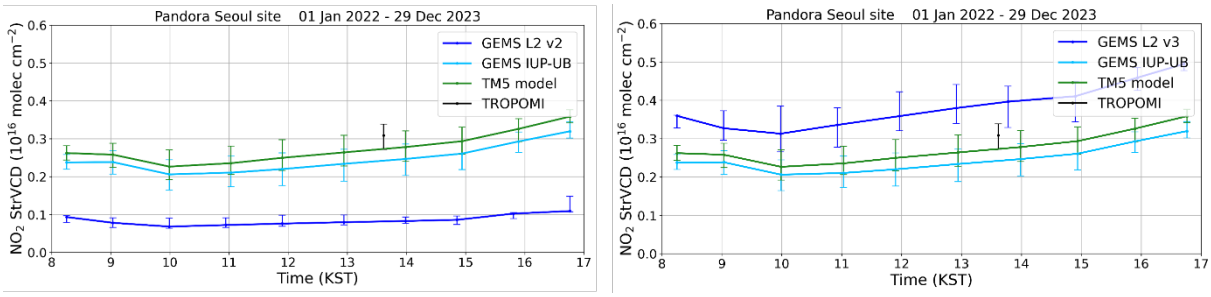


Figure 5-9: Diurnal variation in median stratospheric NO_2 VCDs at the Pandora Seoul site for the TROPOMI product, shown as the black dot, the TM5 model stratospheric VCDs in green, used for the TROPOMI product, the GEMS IUP-UB STREAM-based product in light blue, and the GEMS L2 v2.0 (left plot) and v3.0 (right plot) product based on the method from Bucsela et al. (2013) in dark blue.

The GEMS IUP-UB STREAM-based stratospheric VCDs show very similar diurnal variation and are only slightly lower than the TM5 stratospheric columns, which are used in the TROPOMI product. In the old GEMS NO_2 L2 v2.0 product, stratospheric columns were around a factor of 2.5 lower. After the updates within the GEMS L2 v3.0 product, the v3.0 stratospheric VCDs show a more similar diurnal cycle and a much higher stratospheric column than in v2.0, which is the highest of the products shown. These results are in line with the more detailed analysis presented in section 4.

5.5 Validation

The GEMS tropospheric NO_2 VCDs are compared with collocated Pandora and campaign-based MAX-DOAS tropospheric NO_2 VCD measurements within the GEMS domain. The locations of the Pandora and MAX-DOAS instruments used are shown in Figure 5-10.

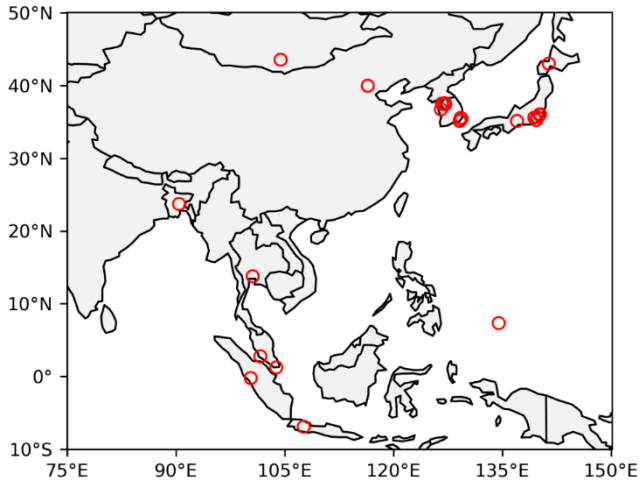


Figure 5-10: Map of Pandora and MAX-DOAS instruments in the GEMS observation domain used for analysis.

Data from 22 Pandora instruments located in the GEMS domain and operated in multi-axis mode are used. Additionally, data from six MAX-DOAS instruments in South Korea are included. Since these MAX-DOAS instruments were campaign-based, they provide data only for parts of 2022. Pandora data are processed as part of the Pandonia Global Network (PGN, https://www.pandonia-global-network.org/home/). The MAX-DOAS tropospheric NO_2 VCDs used in this study were retrieved by applying the Mexican MAX-DOAS Fit (MMF; Friedrich et al. (2019)) inversion algorithm using the FRM4DOAS (v01.01, https://frm4doas.aeronomie.be/) settings and setup.

For validation, stationary ground-based tropospheric NO_2 VCDs are averaged within ± 20min of the satellite overpass and compared with the closest satellite pixels extracted within a 5 km radius around the station sites.

As shown in section 5.2, the comparison of GEMS and ground-based NO_2 VCD revealed that the GEMS L2 v3.0 BSR product introduces an overestimation of the NO_2 tropospheric VCDs compared to the ground-based observations and has significantly more scatter compared to the GEMS IUP-UB product based on the TROPOMI LER.

Figure 5-11 shows the diurnal variation of the median relative differences of the GEMS IUP-UB NO_2 product using the GEMS BSR v3.0, the TROPOMI LER v1-1, the TROPOMI LER v2-2, respectively, the MODIS BRDF-based LER, and the ground-based stations for the different seasons.

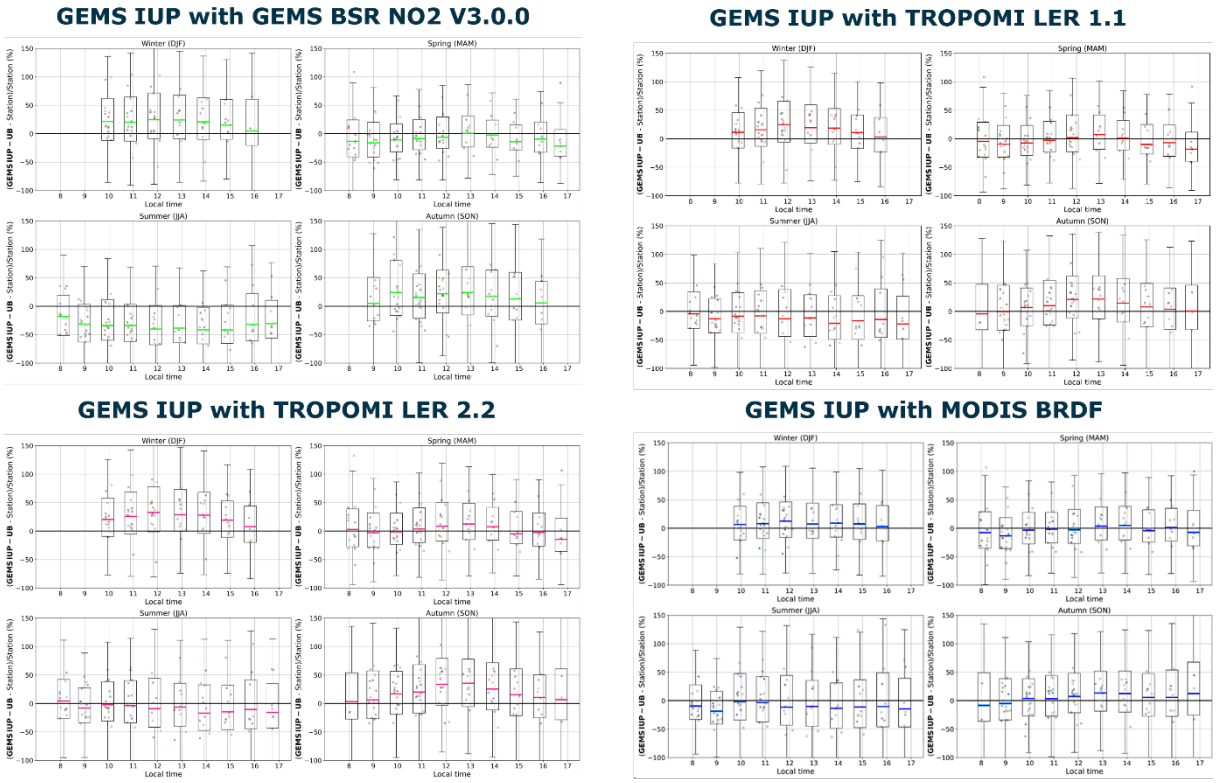


Figure 5-11: Diurnal variation in the median relative differences of the GEMS IUP-UB NO_2 product using the GEMS BSR v3.0 (top left), the TROPOMI LER v1-1 (top right), the TROPOMI LER v2-2 (bottom left), respectively the MODIS BRDF-based LER (bottom right), and the ground-based stations for the different seasons. The overall median for each time bin, including the individual differences of all sites, is shown in green, red, pink, and blue. The individual station median in the time bin is color-coded. Box bounds mark the 25% and 75% quantiles. Whiskers represent the 5% and 95% quantiles.

The largest bias between the GEMS and ground-based NO_2 columns is observed for the GEMS IUP-UB product based on the GEMS BSR v3.0 product. The bias also varies by season and over the day. The GEMS IUP-UB with GEMS BSR v3.0 product is biased high during winter, is closest to the ground-based data in spring, is biased low in summer, and is again biased high in autumn. Additionally, especially in summer and autumn, the bias varies over the day, with smaller differences in the morning and evening and larger biases around noon. The diurnal bias variations observed in summer and autumn show opposite patterns, leading to their cancellation in yearly means. The two GEMS IUP-UB NO_2 products with TROPOMI LER show less bias variation, especially in summer. However, winter and autumn observations are also biased high. The best agreement is found for the GEMS IUP-UB NO_2 product using the MODIS BRDF-based LER. This product version shows much less bias variation across seasons and over the day.

5.6 Algorithm selection

Based on the results of the sensitivity studies performed and reported in this document, the following choices were made for the GEMS algorithm to be used in the project:

Table 5-1: Algorithm choices for the Precursors GEMS NO_2 product. The comment column gives the reason for the choice

Component	Choice	Comment
Slant column	IUP Bremen	Quality
Stratospheric correction	TM5 + offset	Quality and consistency
Surface reflectance	TROPOMI LER v2.2	Consistency
A priori profiles	CAMS Reanalysis	Consistency
Cloud fraction	IUP Bremen	Quality
Cloud pressure	GEMS v3.0	Availability

The choices are a compromise between the best results found in the validation, the availability of data at the time of writing, and good consistency with the other data products created in the project.

6 Summary and Conclusions

In this report, the results of additional evaluations on algorithm choices for products of the Precursors CCI+ project are summarised.

Directional dependencies in surface reflectance are now represented in different databases, including the TROPOMI DLER database, the TROPOMI GE_LER database and the MODIS BRDF based DLER evaluated for GEMS. The two databases DLER and GE_LER are qualitatively consistent, but differences exist in the minLER values, the angular dependency, and the behaviour over snow and ice. Including directional effects in the AMF and cloud parameter calculation leads to moderate changes in the NO_2 columns and to small changes for HCHO. Initial validation results show improved cloud top heights when using directionally dependent surface reflectance and reduced scatter of NO_2 results at large columns, albeit with clearly larger underestimation. Validation results have to be considered with care as other algorithm parameters have changed as well. For GEMS, small but a systematic improvement of NO_2 validation results was found when using the MODIS BRDF based reflectance.

Several stratospheric correction approaches for GEMS NO_2 yielded comparable results. Model based algorithms perform well but can be improved by applying empirical offsets. The classical STREAM algorithm is not well suited for geostationary observation. The deviant STREAM-UB performs well but shows jumps when the GEMS FOV changes, which is not ideal. Simple empirical corrections may also be possible but still need additional work.

For the GEMS NO_2 product, components from the GEMS operational processor (cloud pressure) will be combined with data from the GEMS IUP product (slant columns, cloud fractions), combined with TROPOMI LER and CAMS reanalysis a priori. The latter two choices were driven by an attempt to be as consistent as possible with other Precursor CCI+ products.

For the future, further convergence between TROPOMI DLER and GE_LER should be pursued, including comparisons to the MODIS BRDF based DLER. If good agreement is achieved between these databases, GEMS retrievals should switch to MODIS (or VIIRS) BRDF based DLER.

Separation between the stratosphere and the troposphere is more challenging for S4 than for GEMS and TEMPO because of higher latitudes and the proximity of the Polar Vortex in spring. Therefore, stratospheric correction algorithms should be revisited once S4 data is included in the project.

7 References

Beirle, S., Hörmann, C., Jöckel, P., Liu, S., Penning de Vries, M., Pozzer, A., Sihler, H., Valks, P., and Wagner, T.: The STRatospheric Estimation Algorithm from Mainz (STREAM): estimating stratospheric NO2 from nadir-viewing satellites by weighted convolution, Atmos. Meas. Tech., 9, 2753-2779, doi:10.5194/amt-9-2753-2016, 2016.

Bucsela, E. J., Krotkov, N. A., Celarier, E. A., Lamsal, L. N., Swartz, W. H., Bhartia, P. K., Boersma, K. F., Veefkind, J. P., Gleason, J. F., and Pickering, K. E.: A new stratospheric and tropospheric NO2 retrieval algorithm for nadir-viewing satellite instruments: applications to OMI, Atmos. Meas. Tech., 6, 2607–2626, https://doi.org/10.5194/amt-6-2607-2013, 2013.

Chan, K. L., Xu, J., Slijkhuis, S., Valks, P., & Loyola, D., TROPOspheric Monitoring Instrument observations of total column water vapour: Algorithm and validation. Science of the Total Environment, 821, 153232, 2020.

Compernolle, S., Argyrouli, A., Lutz, R., Sneep, M., Lambert, J.-C., Fjæraa, A. M., Hubert, D., Keppens, A., Loyola, D., O'Connor, E., Romahn, F., Stammes, P., Verhoelst, T. and Wang, P.: Validation of the Sentinel-5 Precursor TROPOMI cloud data with Cloudnet, Aura OMI O2-O2, MODIS, and Suomi-NPP VIIRS Atmos. Meas. Tech., 14, 2451-2476, https://doi.org/10.5194/amt-14-2451-2021., 2021

Eskes, H. and Eichmann K.-U., ATM-MPC Mission Performance Cluster Nitrogen Dioxide [L2__NO2___] Readme, issue 2.9, available at https://sentiwiki.copernicus.eu/web/s5p-products, 2025-11-27.

Fasnacht, Z., Vasilkov, A., Haffner, D., Qin, W., Joiner, J., Krotkov, N., Sayer, A. M., & Spurr, R., A geometry-dependent surface Lambertian-equivalent reflectivity product for UV/Vis retrievals: Part II. Evaluation over open ocean. *Atmospheric Measurement Techniques Discussions*, (July), 1–33. https://doi.org/10.5194/amt-2019-260, 2017.

Flaud, J.-M., Camy-Peyret, C., Brault, J. W., Rinsland, C. P., and Cariolle, D.: Nighttime and daytime variation of atmospheric NO2 from ground-based infrared measurements, Geophysical Research Letters, 15, 261–264, https://doi.org/10.1029/GL015i003p00261, 1988.

Friedrich, M. M., Rivera, C., Stremme, W., Ojeda, Z., Arellano, J., Bezanilla, A., García-Reynoso, J. A., and Grutter, M.: NO2 vertical profiles and column densities from MAX-DOAS measurements

in Mexico City, Atmos. Meas. Tech., 12, 2545–2565, https://doi.org/10.5194/amt-12-2545-2019, 2019.

Gil, M., Yela, M., Gunn, L. N., Richter, A., Alonso, I., Chipperfield, M. P., Cuevas, E., Iglesias, J., Navarro, M., Puentedura, O., and Rodríguez, S.: NO2 climatology in the northern subtropical region: diurnal, seasonal and interannual variability, Atmos. Chem. Phys., 8, 1635–1648, https://doi.org/10.5194/acp-8-1635-2008, 2008.

Jöckel, P., Tost, H., Pozzer, A., Kunze, M., Kirner, O., Brenninkmeijer, C. A. M., Brinkop, S., Cai, D. S., Dyroff, C., Eckstein, J., Frank, F., Garny, H., Gottschaldt, K.-D., Graf, P., Grewe, V., Kerkweg, A., Kern, B., Matthes, S., Mertens, M., Meul, S., Neumaier, M., Nützel, M., Oberländer-Hayn, S., Ruhnke, R., Runde, T., Sander, R., Scharffe, D., and Zahn, A. (2016). Earth System Chemistry integrated Modelling (ESCiMo) with the Modular Earth Submodel System (MESSy) version 2.51. Geoscientific Model Development, 9(3):1153–1200. DOI:10.5194/gmd-9-1153-2016.

Kim, B.-R., Kim, G., Cho, M., Choi, Y.-S., and Kim, J.: First results of cloud retrieval from the Geostationary Environmental Monitoring Spectrometer, Atmos. Meas. Tech., 17, 453–470, https://doi.org/10.5194/amt-17-453-2024, 2024.

Lambert, J.-C., A. Keppens, S. Compernolle, K.-U. Eichmann, M. de Graaf, D. Hubert, B. Langerock, A. Ludewig, M.K. Sha, T. Verhoelst, T. Wagner, C. Ahn, A. Argyrouli, D. Balis, K.L. Chan, M. Coldewey-Egbers, I. De Smedt, H. Eskes, A.M. Fjæraa, K. Garane, J.F. Gleason, F. Goutail, J. Granville, P. Hedelt, K.-P. Heue, G. Jaross, Q. Kleipool, ML. Koukouli, A. Lorente Delgado, R. Lutz, K. Michailidis, S. Nanda, S. Niemeijer, A. Pazmiño, G. Pinardi, J.-P. Pommereau, A. Richter, N. Rozemeijer, M. Sneep, D. Stein Zweers, N. Theys, G. Tilstra, O. Torres, P. Valks, J. van Geffen, C. Vigouroux, P. Wang, and M. Weber: Quarterly Validation Report of the Copernicus Sentinel-5 Precursor Operational Data Products #17: April 2018 – November 2022. S5P MPC Routine Operations Consolidated Validation Report series, Issue #17, Version 17.01.00, 225 pp., available at https://mpc-vdaf.tropomi.eu/, 16 December 2022.

Lange, K., Richter, A., Bösch, T., Zilker, B., Latsch, M., Behrens, L. K., Okafor, C. M., Bösch, H., Burrows, J. P., Merlaud, A., Pinardi, G., Fayt, C., Friedrich, M. M., Dimitropoulou, E., Van Roozendael, M., Ziegler, S., Ripperger-Lukosiunaite, S., Kuhn, L., Lauster, B., Wagner, T., Hong, H., Kim, D., Chang, L.-S., Bae, K., Song, C.-K., Park, J.-U., and Lee, H.: Validation of GEMS tropospheric NO2 columns and their diurnal variation with ground-based DOAS measurements, Atmos. Meas. Tech., 17, 6315–6344, https://doi.org/10.5194/amt-17-6315-2024, 2024.

Lee et al., Geostationary Environment Monitoring Spectrometer (GEMS) Algorithm Theoretical Basis Document: NO2 Retrieval Algorithm, https://nesc.nier.go.kr/en/html/satellite/doc/doc.do, 2024.

Li, K.-F., Khoury, R., Pongetti, T. J., Sander, S. P., Mills, F. P., and Yung, Y. L.: Diurnal variability of stratospheric column NO_2 measured using direct solar and lunar spectra over Table Mountain, California (34.38° N), Atmos. Meas. Tech., 14, 7495–7510, https://doi.org/10.5194/amt-14-7495-2021, 2021.

Lorente, A., Folkert Boersma, K., Yu, H., Dörner, S., Hilboll, A., Richter, A., Liu, M., Lamsal, L. N., Barkley, M., De Smedt, I., Van Roozendael, M., Wang, Y., Wagner, T., Beirle, S., Lin, J.-T., Krotkov, N., Stammes, P., Wang, P., Eskes, H. J., and Krol, M.: Structural uncertainty in air mass factor calculation for NO2 and HCHO satellite retrievals, Atmos. Meas. Tech., 10, 759–782, https://doi.org/10.5194/amt-10-759-2017, 2017.

Lorente, A., Boersma, K. F., Stammes, P., Tilstra, L. G., Richter, A., Yu, H., Kharbouche, S., and Muller, J.-P.: The importance of surface reflectance anisotropy for cloud and NO2 retrievals from GOME-2 and OMI, Atmos. Meas. Tech., 11, 4509–4529, https://doi.org/10.5194/amt-11-4509-2018, 2018.

Loyola, D. G., Pedergnana, M., and Gimeno García, S.: Smart sampling and incremental function learning for very large high dimensional data, Neural Networks, 78, 75–87, https://doi.org/10.1016/j.neunet.2015.09.001, 2016.

Loyola, D. G., Xu, J., Heue, K.-P., and Zimmer, W.: Applying FP_ILM to the retrieval of geometry-dependent effective Lambertian equivalent reflectivity (GE_LER) daily maps from UVN satellite measurements, Atmos. Meas. Tech., 13, 985–999, https://doi.org/10.5194/amt-13-985-2020, 2020.

Lutz, R., Romahn, F., Compernolle, S., Lambert, J.-C., ATM-MPC Mission Performance Cluster CLOUD [L2__CLOUD_] Readme, issue 2.11, available at https://sentiwiki.copernicus.eu/web/s5p-products, , 2025-11-27

Sim, S., Choi, S., Jung, D., Woo, J., Kim, N., Park, S., Kim, H., Jeong, U., Hong, H., and Han, K.-S.: Retrieval of pseudo-BRDF-adjusted surface reflectance at 440 nm from the Geostationary Environmental Monitoring Spectrometer (GEMS), Atmos. Meas. Tech., 17, 5601–5618, https://doi.org/10.5194/amt-17-5601-2024, 2024.

Spurr, R., LIDORT and VLIDORT: Linearized pseudo-spherical scalar and vector discrete ordinate radiative transfer models for use in remote sensing retrieval problems. In Light scattering reviews 3: Light scattering and reflection (pp. 229-275). Berlin, Heidelberg: Springer Berlin Heidelberg, 2008.

Stammes, P., IRS 2000: Current Problems in Atmospheric Radiation. A. Deepak Publ., Hampton, VA, 385-388, 2001.

Starr, J., Zhang, J., Reid, J. S., & Roberts, D. C., Albedo impacts of changing agricultural practices in the United States through Space-Borne analysis. Remote Sensing, 12(18), 288, 20207.

Sussmann, R., Stremme, W., Burrows, J. P., Richter, A., Seiler, W., and Rettinger, M.: Stratospheric and tropospheric NO_2 variability on the diurnal and annual scale: a combined retrieval from ENVISAT/SCIAMACHY and solar FTIR at the Permanent Ground-Truthing Facility Zugspitze/Garmisch, Atmos. Chem. Phys., 5, 2657–2677, https://doi.org/10.5194/acp-5-2657-2005, 2005.

Tilstra, L. G., de Graaf, M., Trees, V. J. H., Litvinov, P., Dubovik, O., and Stammes, P.: A directional surface reflectance climatology determined from TROPOMI observations, Atmos. Meas. Tech., 17, 2235–2256, https://doi.org/10.5194/amt-17-2235-2024, 2024.

van Geffen, J., Eskes, H., Compernolle, S., Pinardi, G., Verhoelst, T., Lambert, J.-C., Sneep, M., ter Linden, M., Ludewig, A., Boersma, K. F., and Veefkind, J. P.: Sentinel-5P TROPOMI NO2 retrieval: impact of version v2.2 improvements and comparisons with OMI and ground-based data, Atmos. Meas. Tech., 15, 2037–2060, https://doi.org/10.5194/amt-15-2037-2022, 2022.

Verhoelst, T., Compernolle, S., Pinardi, G., Lambert, J.-C., Eskes, H. J., Eichmann, K.-U., Fjæraa, A. M., Granville, J., Niemeijer, S., Cede, A., Tiefengraber, M., Hendrick, F., Pazmi no, A., Bais, A., Bazureau, A., Boersma, K. F., Bognar, K., Dehn, A., Donner, S., Elokhov, A., Gebetsberger, M., Goutail, F., Grutter de la Mora, M., Gruzdev, A., Gratsea, M., Hansen, G. H., Irie, H., Jepsen, N.,

Kanaya, Y., Karagkiozidis, D., Kivi, R., Kreher, K., Levelt, P. F., Liu, C., Müller, M., Navarro Comas, M., Piters, A. J. M., Pommereau, J.-P., Portafaix, T., Prados-Roman, C., Puentedura, O., Querel, R., Remmers, J., Richter, A., Rimmer, J., Rivera Cárdenas, C., Saavedra de Miguel, L., Sinyakov, V. P., Stremme, W., Strong, K., Van Roozendael, M., Veefkind, J. P., Wagner, T., Wittrock, F., Yela González, M. & Zehner, C.: Ground-based validation of the Copernicus Sentinel-5P TROPOMI NO2 measurements with the NDACC ZSL-DOAS, MAX-DOAS and Pandonia global networks, Atmos. Meas. Tech., 14, 481-510. https://doi.org/10.5194/amt-14-481-2021, 2021.

Williams, J. E., Boersma, K. F., Le Sager, P., and Verstraeten, W. W.: The high-resolution version of TM5-MP for optimized satellite retrievals: description and validation, Geosci. Model Dev., 10, 721–750, https://doi.org/10.5194/gmd-10-721-2017, 2017.

Zien, A. W., Richter, A., Hilboll, A., Blechschmidt, A.-M., and Burrows, J. P.: Systematic analysis of tropospheric NO2 long-range transport events detected in GOME-2 satellite data, Atmos. Chem. Phys. , 14 , 7367-7396, doi:10.5194/acp-14-7367-2014, 2014